Circuit Modeling of Near-Field Coupled Undersea Antennas Using Impedance Double Expansion Method

Nozomi Haga, *Member, IEEE*, Jerdvisanop Chakarothai, *Senior Member, IEEE*, and Keisuke Konno, *Member, IEEE*

***Abstract*— This study addresses circuit modeling of near-field coupled antennas that are separately enclosed in lossless dielectrics and immersed in seawater, which are intended for applications such as undersea wireless power transfer (WPT) systems. To accomplish this, a circuit modeling technique called the impedance expansion method (IEM) is extended to consider lossy dielectrics with a loss tangent greater than unity. Unlike the conventional IEM, the extended method first expands the coefficient matrices derived by the method of moments (MoM) into the Laurent series with respect to propagation constants and then further expands them with respect to the complex angular frequency. Based on this feature, the extended method is called the impedance double expansion method (IDEM). By applying the IDEM to the undersea dipole and loop antennas with pure water covers, their circuit models are obtained. Comparison with the full-wave MoM and finite-difference time-domain (FDTD) calculations shows that these circuit models reasonably approximate not only the reflection and transmission coefficients between the antennas with matching circuits (MCs) but also the radiation loss.**

***Index Terms*— Dielectric losses, equivalent circuits, method of moments (MoM), wireless power transmission.**

I. Introduction

THE *IEEE Standard for Definitions of Terms for Antennas* [1] states the following.

> The term *antenna* is sometimes used for electromagnetic devices that couple over distances less than that associated with radiated fields.

This article refers to antennas in the above sense as "near-field coupled antennas." Near-field coupled antennas are often used in wireless power transfer (WPT) systems [2], [3], [4], [5]. This trend is more pronounced in undersea WPT systems because the attenuation of electromagnetic waves in seawater is significant and far-field power transmission is impractical.

Various theoretical analyses have been conducted to understand the operating principle of undersea antennas. For example, the input admittance of a dipole antenna and input impedance of a loop antenna in a lossy dielectric were derived in the form of power series with respect to the phase constant, and these results are quite thought-provoking [6], [7].

To prevent corrosion and suppress losses due to seawater, it is common to enclose the antenna conductors in low-loss dielectrics [8]. Theoretical analyses of such antennas have also been performed. For example, the input impedance of a dipole antenna in a lossy dielectric covered by a low-loss dielectric was obtained using the transmission line theory [9]. In addition, the input impedance of a loop antenna enclosed in a spherical low-loss dielectric was obtained by applying the quasistatic approximation within the sphere [10]. Furthermore, the circuit model and input impedance of a dipole antenna partially covered by a low-loss dielectric were obtained by approximating the parts exposed to seawater as spheroids and then performing a scalar potential analysis [11]. However, the aforementioned theoretical analyses can only be applied to a limited number of objects.

In WPT applications, the circuit modeling of antennas is more important because it enables a unified design of antennas and electronic circuits. For example, in electrically coupled WPT systems, the well-known formula for the conductances of parallel-plate electrodes is often used [12], [13]. However, this approach has limitations in dealing with the presence of low-loss dielectrics and electrodes with arbitrary shapes. On the other hand, to determine the self- and mutual inductances of coils in magnetically coupled WPT systems, Neumann's formula is commonly used [14], [15]. However, the physical basis for applying this method to cases where seawater and low-loss dielectric coexist is unclear. Furthermore, there is no established method for expressing losses caused by eddy currents in seawater using circuit models. For example, an interesting circuit model in which the coil current and eddy currents in seawater are inductively coupled has been reported to represent the frequency dependence of the losses caused by eddy currents [16]. However, how to determine its circuit parameters is unclear.

Therefore, a generic circuit modeling method that can be applied to both electrically and magnetically coupled undersea

Received 8 June 2023; revised 15 September 2024; accepted 21 October 2024. Date of publication 30 October 2024; date of current version 19 December 2024. This work was supported by the Japan Society for the Promotion of Science Grants-in-Aid for Scientific Research (JSPS KAKENHI) under Grant 19K04321 and Grant 23K03812. *(Corresponding author: Nozomi Haga.)*

Nozomi Haga is with the Department of Electrical and Electronic Information Engineering, Toyohashi University of Technology, Toyohashi 441-8580, Japan (e-mail: haga.nozomi.ok@tut.jp).

Jerdvisanop Chakarothai is with the National Institute of Information and Communications Technology, Koganei 184-8795 Japan (e-mail: jerd@nict.go.jp).

Keisuke Konno is with the Department of Communications Engineering, Graduate School of Engineering, Tohoku University, Sendai 980-8579, Japan (e-mail: keisuke.konno.b5@tohoku.ac.jp).

Color versions of one or more figures in this article are available at https://doi.org/10.1109/TAP.2024.3485793.

Digital Object Identifier 10.1109/TAP.2024.3485793

antennas involving low-loss dielectrics with arbitrary shapes is required. One candidate for this purpose is the impedance expansion method (IEM) [17], which is a circuit modeling technique based on the Laurent series expansion of impedance matrices derived by the method of moments (MoM) [18]. So far, the IEM has undergone several extensions and has been applied to circuit modeling of WPT systems in free space [19] and those involving perfectly conducting scatterers [20] and lossless dielectric/magnetic bodies [21]. In this study, the IEM is further extended to consider lossy dielectrics with loss tangents greater than unity, including not only seawater but also biological tissues. Low-loss dielectrics with a loss tangent less than unity are beyond the scope of this article and are left for future studies. The conventional IEM directly expands the coefficient matrices with respect to the complex angular frequency, whereas the extended method first expands the coefficient matrices with respect to the propagation constant and then further expands them with respect to the complex angular frequency. Based on this feature, the extended method is hereafter called the impedance double expansion method (IDEM). The IDEM is applied to near-field coupled undersea dipole and loop antennas enclosed in pure water covers, wherein the effects of the covers on circuit parameters are clarified.

In the circuit models produced by the conventional IEM, the unknowns are limited to the currents of antennas, whereas the effects of adjacent scatterers are represented as changes in the circuit parameters. This property inherited by the IDEM is an advantage over other circuit modeling techniques such as the partial-element equivalent-circuit method [22], [23]. In addition, the circuit models produced by the IDEM have an advantage in that the internal impedances of antenna conductors, static resistances due to lossy dielectrics, impedance components representing eddy current, and radiation losses are decomposed, allowing them to be separately evaluated.

This section concludes with a discussion of the applicability of the IDEM to other applications. Wireless charging of pacemakers is technically similar to undersea WPT systems, and circuit modeling of such systems is common [24], [25]. Combining the IDEM with the IEM extended in [20] can consider not only inductance changes due to eddy currents on the metallic case but also losses due to eddy currents in the human body, which have not been considered in previous studies.

Intrabody communications (IBCs) are another potential application of the IDEM. Previous studies have attempted circuit modeling of IBCs by distributed-element theory [26], static potential analysis using the MoM [27], and fitting using measured data [28], where the first two of these cannot handle inductances, and the last one describes only the receiving characteristics at a single frequency. In contrast to them, the IDEM has the potential to perform circuit modeling with higher accuracy. However, at the current stage, the IDEM cannot consider the situation where the electrodes and the human body are in contact, and it requires further extension.

In contrast, applications using far fields, including undersea communication systems [29] and position estimation

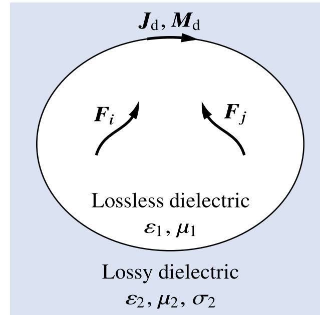

Fig. 1. Basis functions $\boldsymbol{F}_i$ and $\boldsymbol{F}_j$ inside a lossless dielectric immersed in a lossy dielectric.

systems [30], are beyond the scope of the IDEM because the applicability of the IDEM is limited to electrically small objects, as will be clarified in the following discussions.

The rest of this article is organized as follows: Section II derives the theory of the IDEM; Section III discusses the frequency range over which the IDEM can be applied; Section IV presents the resulting circuit models of undersea dipole and loop antennas; and Section V concludes this article.

II. Theory

A. Overview

As shown in Fig. 1, basis functions $\boldsymbol{F}_i$ and $\boldsymbol{F}_j$, which represent antenna currents, are assumed to be inside a lossless dielectric with permittivity ε_1 and permeability μ_1, immersed in a lossy dielectric of infinite volume with permittivity ε_2, permeability μ_2, and conductivity σ_2. By expanding the self-/mutual impedance Z_{ij} between $\boldsymbol{F}_i$ and $\boldsymbol{F}_j$ into the Laurent series with respect to the complex angular frequency s, the circuit model of mutually coupled antennas is obtained. For example, the impedance components proportional to s^{-1}, s^0, and s are represented by capacitances, resistances, and inductances, respectively. The IDEM is formulated to find the self-/mutual impedances including the effect of the exterior lossy dielectric. Since the formulation for multiple lossless dielectrics is obvious, it is not presented here. This theory can be applied without any modification to cases where a lossy dielectric of finite volume is in free space, whereas the basis functions $\boldsymbol{F}_i$ and $\boldsymbol{F}_j$ are placed outside the lossy dielectric.

The self-/mutual impedance Z_{ij} between $\boldsymbol{F}_i$ and $\boldsymbol{F}_j$ can be decomposed as follows:

$$Z_{ij} = Z_{ij}^{\mathrm{fs}} + Z_{ij}^{\mathrm{sc}}. \tag{1}$$

The free-space component Z_{ij}^{fs} is the self-/mutual impedance assuming that all of the space is filled with the lossless dielectric and can be expanded as follows [20] and [21]:

$$Z_{ij}^{\mathrm{fs}} = \sum_{k=-1}^{\infty} s^k Z_{ij}^{\mathrm{fs}(k)} \tag{2}$$

where $Z_{ij}^{\mathrm{fs}(k)}$ is the coefficient for s^k and $Z_{ij}^{\mathrm{fs}(0)} = 0$. In addition, if $\boldsymbol{F}_i$ or $\boldsymbol{F}_j$ are solenoidal, then $Z_{ij}^{\mathrm{fs}(-1)} = Z_{ij}^{\mathrm{fs}(2)} = 0$. On the other hand, the scattering component Z_{ij}^{sc} is due to scattering by the surrounding lossy dielectric and can be obtained through the following steps.

1) Assuming $I_j \boldsymbol{F}_j$ to be an electric current source (I_j is the electric current coefficient for $\boldsymbol{F}_j$), the equivalent electric and magnetic current densities $\boldsymbol{J}_\mathrm{d}$ and $\boldsymbol{M}_\mathrm{d}$, respectively, induced on the boundary between the lossless and lossy dielectrics are obtained in the form of the Taylor/Laurent series with respect to $s^{1/2}$.
2) The scattered electric field produced by the equivalent electric and magnetic currents in the form of the Laurent series with respect to $s^{1/2}$ is tested by $\boldsymbol{F}_i$.

As a result, Z_{ij}^{sc} can be obtained in the following form:

$$Z_{ij}^{\mathrm{sc}} = \sum_{k=-2}^{\infty} s^{k/2} Z_{ij}^{\mathrm{fs}(k/2)} \tag{3}$$

where $Z_{ij}^{\mathrm{sc}(k/2)}$ is the coefficient for $s^{k/2}$ and $Z_{ij}^{\mathrm{sc}(-1/2)} = Z_{ij}^{\mathrm{sc}(1/2)} = 0$. In addition, if $\boldsymbol{F}_i$ or $\boldsymbol{F}_j$ are solenoidal, then $Z_{ij}^{\mathrm{sc}(-1)} = Z_{ij}^{\mathrm{sc}(0)} = Z_{ij}^{\mathrm{sc}(3/2)} = 0$. Whereas Z_{ij}^{fs} and Z_{ij}^{sc} in [20] and [21] are expanded into the same form only with integer powers of s as in (2), those in the IDEM are expanded into different forms, which is due to the conductive nature of the exterior lossy dielectric. In particular, the scattering component includes a static resistance component $Z_{ij}^{\mathrm{sc}(0)}$, and the quadratic component $Z_{ij}^{\mathrm{sc}(2)}$ is nonzero even if $\boldsymbol{F}_i$ or $\boldsymbol{F}_j$ are solenoidal because of eddy current losses. Details of the theory are explained in the rest of this section.

B. Matrix Equations for Equivalent Currents

To obtain $\boldsymbol{J}_\mathrm{d}$ and $\boldsymbol{M}_\mathrm{d}$ that are induced by $I_j \boldsymbol{F}_j$, the Poggio–Miller–Chang–Harrington–Wu–Tsai (PMCHWT) integral equations [31] are discretized as in [21]. To avoid rank deficiency of coefficient matrices, $\boldsymbol{J}_\mathrm{d}$ and $\boldsymbol{M}_\mathrm{d}$ are expanded into the loop-star basis functions [32], [33] as follows:

$$\boldsymbol{J}_\mathrm{d} = \sum_{j=1}^{N_\star} I_j^\star \boldsymbol{F}_j^\star + \sum_{j=1}^{N_\circ} I_j^\circ \boldsymbol{F}_j^\circ \tag{4}$$

$$\boldsymbol{M}_\mathrm{d} = \sum_{j=1}^{N_\star} V_j^\star \boldsymbol{F}_j^\star + \sum_{j=1}^{N_\circ} V_j^\circ \boldsymbol{F}_j^\circ \tag{5}$$

where $\boldsymbol{F}_j^\star$, $I_j^\star$, and $V_j^\star$ are the jth star basis function, electric, and magnetic current coefficients, respectively, whereas $\boldsymbol{F}_j^\circ$, I_j°, and V_j° are the jth loop (solenoidal) basis function, electric, and magnetic current coefficients, respectively. Substituting (4) and (5) into the PMCHWT integral equations satisfied on the boundary between the dielectrics and applying Galerkin's method yields

$$\begin{bmatrix} \bar{\mathbf{Z}}_{\star\star} & \bar{\mathbf{U}}_{\star\circ} \\ \bar{\mathbf{U}}_{\circ\star} & -\bar{\mathbf{Y}}_{\circ\circ} \end{bmatrix} \begin{bmatrix} \mathbf{I}_\star \\ \mathbf{V}_\circ \end{bmatrix} + \begin{bmatrix} \bar{\mathbf{Z}}_{\star\circ} & \bar{\mathbf{U}}_{\star\star} \\ \bar{\mathbf{U}}_{\circ\circ} & -\bar{\mathbf{Y}}_{\circ\star} \end{bmatrix} \begin{bmatrix} \mathbf{I}_\circ \\ \mathbf{V}_\star \end{bmatrix} = -\begin{bmatrix} \mathbf{Z}_{\star j} \\ \mathbf{U}_{\circ j} \end{bmatrix} I_j \tag{6}$$

$$\begin{bmatrix} \bar{\mathbf{Z}}_{\circ\star} & \bar{\mathbf{U}}_{\circ\circ} \\ \bar{\mathbf{U}}_{\star\star} & -\bar{\mathbf{Y}}_{\star\circ} \end{bmatrix} \begin{bmatrix} \mathbf{I}_\star \\ \mathbf{V}_\circ \end{bmatrix} + \begin{bmatrix} \bar{\mathbf{Z}}_{\circ\circ} & \bar{\mathbf{U}}_{\circ\star} \\ \bar{\mathbf{U}}_{\star\circ} & -\bar{\mathbf{Y}}_{\star\star} \end{bmatrix} \begin{bmatrix} \mathbf{I}_\circ \\ \mathbf{V}_\star \end{bmatrix} = -\begin{bmatrix} \mathbf{Z}_{\circ j} \\ \mathbf{U}_{\star j} \end{bmatrix} I_j \tag{7}$$

where $\mathbf{I}_\upsilon$ and $\mathbf{V}_\upsilon$ are $N_\upsilon \times 1$ electric and magnetic current vectors, respectively, whose jth elements are I_j^υ and V_j^υ, respectively; $\bar{\mathbf{Z}}_{\tau\upsilon}$, $\bar{\mathbf{Y}}_{\tau\upsilon}$, and $\bar{\mathbf{U}}_{\tau\upsilon}$ are $N_\tau \times N_\upsilon$ impedance, admittance, and transfer matrices, respectively, whose (i, j)th elements are the self-/mutual impedance, admittance, and transfer coefficient between $\boldsymbol{F}_i^\tau$ and $\boldsymbol{F}_j^\upsilon$, respectively; and $\mathbf{Z}_{\tau j}$ and $\mathbf{U}_{\tau j}$ are $N_\tau \times 1$ impedance and transfer vectors, respectively, whose ith elements are the mutual impedance and transfer coefficient between $\boldsymbol{F}_i^\tau$ and $\boldsymbol{F}_j$, respectively ($\tau, \upsilon = \star, \circ$).

C. Expansion of Matrices and Vectors

In the lossless case in [21], $\bar{\mathbf{Z}}_{\tau\upsilon}$, $\bar{\mathbf{Y}}_{\tau\upsilon}$, and $\bar{\mathbf{U}}_{\tau\upsilon}$ are directly expanded into the Taylor/Laurent series with respect to s. In contrast, the IDEM first expands them into series with respect to the propagation constants, wherein their (i, j)th elements are as follows:

$$\left.\begin{aligned} \left[\bar{\mathbf{Z}}_{\tau\upsilon}\right]_{ij} &= \sum_{k=-1}^{\infty} \left(\zeta_1 \gamma_1^k + \zeta_2 \gamma_2^k\right) X\left(\boldsymbol{F}_i^\tau, \boldsymbol{F}_j^\upsilon, k\right) \\ \left[\bar{\mathbf{Y}}_{\tau\upsilon}\right]_{ij} &= \sum_{k=-1}^{\infty} \left(\frac{\gamma_1^k}{\zeta_1} + \frac{\gamma_2^k}{\zeta_2}\right) X\left(\boldsymbol{F}_i^\tau, \boldsymbol{F}_j^\upsilon, k\right) \\ \left[\bar{\mathbf{U}}_{\tau\upsilon}\right]_{ij} &= \sum_{k=0}^{\infty} \left(\gamma_1^k + \gamma_2^k\right) W\left(\boldsymbol{F}_i^\tau, \boldsymbol{F}_j^\upsilon, k\right) \end{aligned}\right\} \tag{8}$$

where $\zeta_1 = \sqrt{\mu_1/\varepsilon_1}$ and $\zeta_2 = \sqrt{s\mu_2/(\sigma_2 + s\varepsilon_2)}$ are the wave impedances in the lossless and lossy dielectrics, respectively; $\gamma_1 = s\sqrt{\varepsilon_1\mu_1}$ and $\gamma_2 = \sqrt{(\sigma_2 + s\varepsilon_2)s\mu_2}$ are the propagation constants in the lossless and lossy dielectrics, respectively; and $X(\boldsymbol{F}_i^\tau, \boldsymbol{F}_j^\upsilon, k)$ and $W(\boldsymbol{F}_i^\tau, \boldsymbol{F}_j^\upsilon, k)$ are integrals involving $\boldsymbol{F}_i^\tau$ and $\boldsymbol{F}_j^\upsilon$, which are identical to those in [21].

Since ζ_2 depends on s and γ_2 is not linearly proportional to s, the terms containing ζ_2 and γ_2^k in (8) are further expanded using the binomial theorem as follows:

$$\left.\begin{aligned} \zeta_2 \gamma_2^k &= \frac{(s\mu_2\sigma_2)^{(k+1)/2}}{\sigma_2} \sum_{l=0}^{\infty} \binom{(k-1)/2}{l} \left(\frac{s\varepsilon_2}{\sigma_2}\right)^l \\ \frac{\gamma_2^k}{\zeta_2} &= \sigma_2 (s\mu_2\sigma_2)^{(k-1)/2} \sum_{l=0}^{\infty} \binom{(k+1)/2}{l} \left(\frac{s\varepsilon_2}{\sigma_2}\right)^l \\ \gamma_2^k &= (s\mu_2\sigma_2)^{k/2} \sum_{l=0}^{\infty} \binom{k/2}{l} \left(\frac{s\varepsilon_2}{\sigma_2}\right)^l \end{aligned}\right\} \tag{9}$$

all of which converge if $\omega\varepsilon_2 < \sigma_2$, where $\omega = \Im(s)$. In other words, the loss tangent should be greater than 1. Substituting $\zeta_1 = \sqrt{\mu_1/\varepsilon_1}$, $\gamma_1 = s\sqrt{\varepsilon_1\mu_1}$, and (9) into (8) then rearranging, the following expanded expressions can be obtained:

$$\left.\begin{aligned} \bar{\mathbf{Z}}_{\tau\upsilon} &= \sum_{k=-2}^{\infty} s^{k/2} \bar{\mathbf{Z}}_{\tau\upsilon}^{(k/2)}, \quad \bar{\mathbf{Y}}_{\tau\upsilon} = \sum_{k=-2}^{\infty} s^{k/2} \bar{\mathbf{Y}}_{\tau\upsilon}^{(k/2)} \\ \bar{\mathbf{U}}_{\tau\upsilon} &= \sum_{k=0}^{\infty} s^{k/2} \bar{\mathbf{U}}_{\tau\upsilon}^{(k/2)} \end{aligned}\right\}. \tag{10}$$

Specific expressions for the elements of the matrices in (10) are shown in Appendix A.

On the other hand, similar to those in [21], $\mathbf{Z}_{\tau j}$ and $\mathbf{U}_{\tau j}$ in (6) and (7) can be expanded as follows:

$$\mathbf{Z}_{\tau j} = \sum_{k=-1}^{\infty} s^k \mathbf{Z}_{\tau j}^{(k)}, \quad \mathbf{U}_{\tau j} = \sum_{k=0}^{\infty} s^k \mathbf{U}_{\tau j}^{(k)}. \tag{11}$$

In line with the fact that (10) contains components of half-integer degrees with respect to s, $\mathbf{I}_\upsilon$ and $\mathbf{V}_\upsilon$ in (6) and (7) are expanded as follows:

$$\mathbf{I}_\upsilon = \sum_{k=0}^{\infty} s^{k/2} \mathbf{I}_\upsilon^{(k/2)}, \quad \mathbf{V}_\upsilon = \sum_{k=-2}^{\infty} s^{k/2} \mathbf{V}_\upsilon^{(k/2)} \tag{12}$$

where it is assumed that $\mathbf{V}_\star^{(k/2)} = \mathbf{0}$ if $k < 2$.

Substituting (10)–(12) into (6) and (7), the equality holds for each power of $s^{1/2}$, that is,

$$\begin{aligned}&\begin{bmatrix}\bar{\mathbf{Z}}_{\star\star}^{(-1)} & \bar{\mathbf{U}}_{\star\circ}^{(0)}\\ \bar{\mathbf{0}} & -\bar{\mathbf{Y}}_{\circ\circ}^{(0)}\end{bmatrix}\begin{bmatrix}\mathbf{I}_\star^{(k/2)}\\ \mathbf{V}_\circ^{(k/2-1)}\end{bmatrix}\\ &= -\begin{bmatrix}\mathbf{Z}_{\star j}^{(k/2-1)}\\ \mathbf{U}_{\circ j}^{(k/2-1)}\end{bmatrix} I_j - \sum_{l=2}^{k}\begin{bmatrix}\bar{\mathbf{Z}}_{\star\star}^{(l/2-1)} & \bar{\mathbf{U}}_{\star\circ}^{(l/2)}\\ \bar{\mathbf{U}}_{\circ\star}^{(l/2-1)} & -\bar{\mathbf{Y}}_{\circ\circ}^{(l/2)}\end{bmatrix}\begin{bmatrix}\mathbf{I}_\star^{(k/2-l/2)}\\ \mathbf{V}_\circ^{(k/2-l/2-1)}\end{bmatrix}\\ &\quad - \sum_{l=4}^{k}\begin{bmatrix}\bar{\mathbf{Z}}_{\star\circ}^{(l/2-1)} & \bar{\mathbf{U}}_{\star\star}^{(l/2-2)}\\ \bar{\mathbf{U}}_{\circ\circ}^{(l/2-1)} & -\bar{\mathbf{Y}}_{\circ\star}^{(l/2-2)}\end{bmatrix}\begin{bmatrix}\mathbf{I}_\circ^{(k/2-l/2)}\\ \mathbf{V}_\star^{(k/2-l/2+1)}\end{bmatrix}, \quad k \ge 0\end{aligned} \tag{13}$$

$$\begin{aligned}&\begin{bmatrix}\bar{\mathbf{Z}}_{\circ\circ}^{(1)} & \bar{\mathbf{U}}_{\circ\star}^{(0)}\\ \bar{\mathbf{U}}_{\star\circ}^{(0)} & -\bar{\mathbf{Y}}_{\star\star}^{(-1)}\end{bmatrix}\begin{bmatrix}\mathbf{I}_\circ^{(k/2-1)}\\ \mathbf{V}_\star^{(k/2)}\end{bmatrix}\\ &= -\begin{bmatrix}\mathbf{Z}_{\circ j}^{(k/2)}\\ \mathbf{U}_{\star j}^{(k/2-1)}\end{bmatrix} I_j - \sum_{l=0}^{k}\begin{bmatrix}\bar{\mathbf{Z}}_{\circ\star}^{(l/2)} & \bar{\mathbf{U}}_{\circ\circ}^{(l/2+1)}\\ \bar{\mathbf{U}}_{\star\star}^{(l/2-1)} & -\bar{\mathbf{Y}}_{\star\circ}^{(l/2)}\end{bmatrix}\begin{bmatrix}\mathbf{I}_\star^{(k/2-l/2)}\\ \mathbf{V}_\circ^{(k/2-l/2-1)}\end{bmatrix}\\ &\quad - \sum_{l=4}^{k}\begin{bmatrix}\bar{\mathbf{Z}}_{\circ\circ}^{(l/2)} & \bar{\mathbf{U}}_{\circ\star}^{(l/2-1)}\\ \bar{\mathbf{U}}_{\star\circ}^{(l/2-1)} & -\bar{\mathbf{Y}}_{\star\star}^{(l/2-2)}\end{bmatrix}\begin{bmatrix}\mathbf{I}_\circ^{(k/2-l/2)}\\ \mathbf{V}_\star^{(k/2-l/2+1)}\end{bmatrix}, \quad k \ge 2\end{aligned} \tag{14}$$

which correspond to (28) and (29) in [21], respectively, but differ in several points. First, matrices and vectors of half-integer degrees are included. Second, the matrix on the left-hand side of (13) is asymmetric because the lowest degree of $\bar{\mathbf{Y}}_{\circ\circ}^{(k/2)}$ differs from that in the lossless case.

The unknown vectors on the left-hand sides of (13) and (14) can be obtained in the following procedure. First, substituting $k = 0$ into (13) yields

$$\begin{bmatrix}\bar{\mathbf{Z}}_{\star\star}^{(-1)} & \bar{\mathbf{U}}_{\star\circ}^{(0)}\\ \bar{\mathbf{0}} & -\bar{\mathbf{Y}}_{\circ\circ}^{(0)}\end{bmatrix}\begin{bmatrix}\mathbf{I}_\star^{(0)}\\ \mathbf{V}_\circ^{(-1)}\end{bmatrix} = -\begin{bmatrix}\mathbf{Z}_{\star j}^{(-1)}\\ \mathbf{0}\end{bmatrix} I_j \tag{15}$$

which can be solved for $\mathbf{I}_\star^{(0)}$ and $\mathbf{V}_\circ^{(-1)}$. It is obvious that $\mathbf{V}_\circ^{(-1)} = \mathbf{0}$ and $\mathbf{I}_\star^{(0)}$ is determined only by $\bar{\mathbf{Z}}_{\star\star}^{(-1)}$ and $\mathbf{Z}_{\star j}^{(-1)}$. This is similar to the case of perfectly conducting scatterers in [20], which means that lossy dielectrics behave like perfect conductors for electrostatic fields. Then, substituting $k = 1$ into (13) yields

$$\begin{bmatrix}\bar{\mathbf{Z}}_{\star\star}^{(-1)} & \bar{\mathbf{U}}_{\star\circ}^{(0)}\\ \bar{\mathbf{0}} & -\bar{\mathbf{Y}}_{\circ\circ}^{(0)}\end{bmatrix}\begin{bmatrix}\mathbf{I}_\star^{(1/2)}\\ \mathbf{V}_\circ^{(-1/2)}\end{bmatrix} = \begin{bmatrix}\mathbf{0}\\ \mathbf{0}\end{bmatrix} \tag{16}$$

which obviously results in $\mathbf{I}_\star^{(1/2)} = \mathbf{V}_\circ^{(-1/2)} = \mathbf{0}$. For $k \ge 2$, if $\mathbf{I}_\star^{(0)}, \ldots, \mathbf{I}_\star^{(k/2-1)}, \mathbf{V}_\circ^{(-1)}, \ldots, \mathbf{V}_\circ^{(k/2-2)}, \mathbf{I}_\circ^{(0)}, \ldots, \mathbf{I}_\circ^{(k/2-2)}$, and

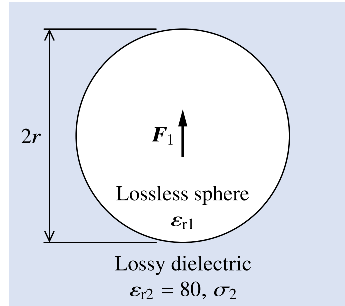

Fig. 2. Basis function $\boldsymbol{F}_1$ inside a lossless dielectric sphere immersed in a lossy dielectric.

$\mathbf{V}_\star^{(1)}, \ldots, \mathbf{V}_\star^{(k/2-1)}$ are known, (13) can be solved for $\mathbf{I}_\star^{(k/2)}$ and $\mathbf{V}_\circ^{(k/2-1)}$. Using $\mathbf{I}_\star^{(k/2)}$ and $\mathbf{V}_\circ^{(k/2-1)}$, (14) can then be solved for $\mathbf{I}_\circ^{(k/2-1)}$ and $\mathbf{V}_\star^{(k/2)}$. This process can be performed sequentially for $k = 2, 3, \ldots$.

D. Testing Scattered Electric Fields

The scattering component Z_{ij}^{sc} can be obtained by testing the scattered field by $\boldsymbol{F}_i$, that is,

$$\begin{aligned}Z_{ij}^{\mathrm{sc}} &= -\frac{1}{I_j}\int_S \boldsymbol{F}_i \cdot \boldsymbol{E}^{\mathrm{sc}} dS\\ &= \frac{1}{I_j}\left\{\begin{bmatrix}\mathbf{Z}_{i\star} & \mathbf{U}_{i\circ}\end{bmatrix}\begin{bmatrix}\mathbf{I}_\star\\ \mathbf{V}_\circ\end{bmatrix} + \begin{bmatrix}\mathbf{Z}_{i\circ} & \mathbf{U}_{i\star}\end{bmatrix}\begin{bmatrix}\mathbf{I}_\circ\\ \mathbf{V}_\star\end{bmatrix}\right\}\end{aligned} \tag{17}$$

where $\boldsymbol{E}^{\mathrm{sc}}$ is the scattered electric field produced by the equivalent electric and magnetic currents, whereas $\mathbf{Z}_{i\upsilon}$ and $\mathbf{U}_{i\upsilon}$ are $1 \times N_\upsilon$ impedance and transfer vectors, respectively, whose jth elements are the mutual impedance and transfer coefficient between $\boldsymbol{F}_i$ and $\boldsymbol{F}_j^\upsilon$, respectively. Similar to those in [21], $\mathbf{Z}_{i\upsilon}$ and $\mathbf{U}_{i\upsilon}$ in (17) can be expanded as follows:

$$\mathbf{Z}_{i\upsilon} = \sum_{k=-1}^{\infty} s^k \mathbf{Z}_{i\upsilon}^{(k)}, \quad \mathbf{U}_{i\upsilon} = \sum_{k=0}^{\infty} s^k \mathbf{U}_{i\upsilon}^{(k)}. \tag{18}$$

Substituting (12) and (18) into (17), $Z_{ij}^{\mathrm{sc}(k/2)}$ in (3) can be obtained as follows:

$$\begin{aligned}Z_{ij}^{\mathrm{sc}(k/2)} = \frac{1}{I_j}&\left\{\sum_{l=-2}^{k}\begin{bmatrix}\mathbf{Z}_{i\star}^{(l/2)} & \mathbf{U}_{i\circ}^{(l/2+1)}\end{bmatrix}\begin{bmatrix}\mathbf{I}_\star^{(k/2-l/2)}\\ \mathbf{V}_\circ^{(k/2-l/2-1)}\end{bmatrix}\right.\\ &\left.+\sum_{l=2}^{k}\begin{bmatrix}\mathbf{Z}_{i\circ}^{(l/2)} & \mathbf{U}_{i\star}^{(l/2-1)}\end{bmatrix}\begin{bmatrix}\mathbf{I}_\circ^{(k/2-l/2)}\\ \mathbf{V}_\star^{(k/2-l/2+1)}\end{bmatrix}\right\}.\end{aligned} \tag{19}$$

III. Applicable Frequency of the IDEM

The applicable frequency of the conventional IEMs in [20] and [21] is limited mainly by the electrical size of the scatterers, whereas that of the IDEM is expected to be limited also by the radius of convergence in (9). Accordingly, this section focuses on both these factors.

As shown in Fig. 2, a lossless dielectric sphere with a radius r and relative permittivity $\varepsilon_{\mathrm{r}1}$ is immersed in a lossy dielectric of infinite volume with relative permittivity $\varepsilon_{\mathrm{r}2} = 80$ and conductivity σ_2. The relative permeability of the lossless and lossy dielectrics is 1. A piecewise linear basis function $\boldsymbol{F}_1$ with

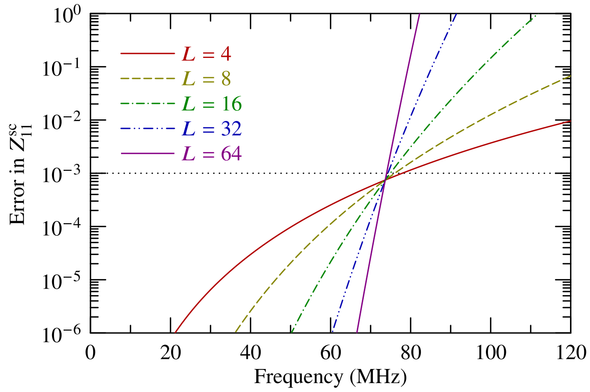

Fig. 3. Frequency dependence of the error in Z_{11}^{sc} at $L = 4$, 8, 16, 32, and 64 ($r = 20$ mm, $\varepsilon_{\mathrm{r1}} = 1$, and $\sigma_2 = 4$ S/m).

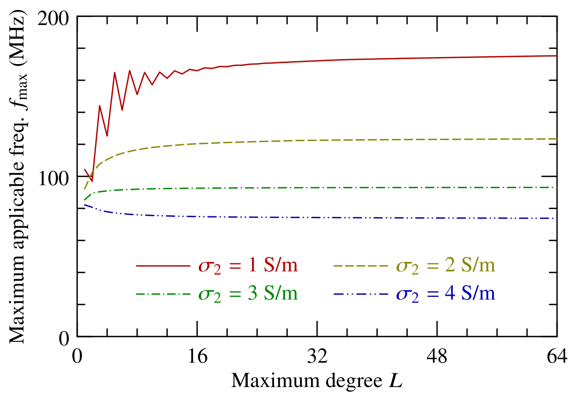

Fig. 4. $f_{\max}$ versus L at $\sigma_2 = 1$, 2, 3, and 4 S/m ($r = 20$ mm and $\varepsilon_{\mathrm{r1}} = 1$).

a length of 10 mm is positioned at the center of the sphere. The numbers of the star and loop basis functions on the surface of the sphere are $N_\star = 863$ and $N_\circ = 865$, respectively.

The scattering component Z_{11}^{sc} is approximated by a series of finite degree L and is denoted by $\tilde{Z}_{11}^{\mathrm{sc}}$ as follows:

$$\tilde{Z}_{11}^{\mathrm{sc}} = \sum_{k=-2}^{2L} s^{k/2} Z_{11}^{\mathrm{sc}(k/2)}. \tag{20}$$

In addition, its full-waveform is obtained by substituting the solution of (6) and (7) into (17). Then, the error defined below is evaluated as

$$\mathrm{Error} = \left|\tilde{Z}_{11}^{\mathrm{sc}}/Z_{11}^{\mathrm{sc}} - 1\right|. \tag{21}$$

Fig. 3 shows the frequency dependence of the error in Z_{11}^{sc} at $L = 4$ to 64 ($r = 20$ mm, $\varepsilon_{\mathrm{r1}} = 1$, and $\sigma_2 = 4$ S/m). Below approximately 74 MHz, the error is smaller for larger L, but its slope is steeper. Thus, regardless of L, the error reaches approximately 10^{-3} at approximately 74 MHz. Based on this observation, the frequency at which the error in Z_{11}^{sc} exceeds the tolerance of 10^{-3} is defined as the maximum applicable frequency $f_{\max}$.

Fig. 4 shows the dependence of $f_{\max}$ on L at $\sigma_2 = 1$, 2, 3, and 4 S/m ($r = 20$ mm and $\varepsilon_{\mathrm{r1}} = 1$). For any value of σ_2, $f_{\max}$ converges to each specific frequency as L increases. Hereafter, $f_{\max}$ at $L = 64$, which can be regarded as a nearly convergent value, will be evaluated.

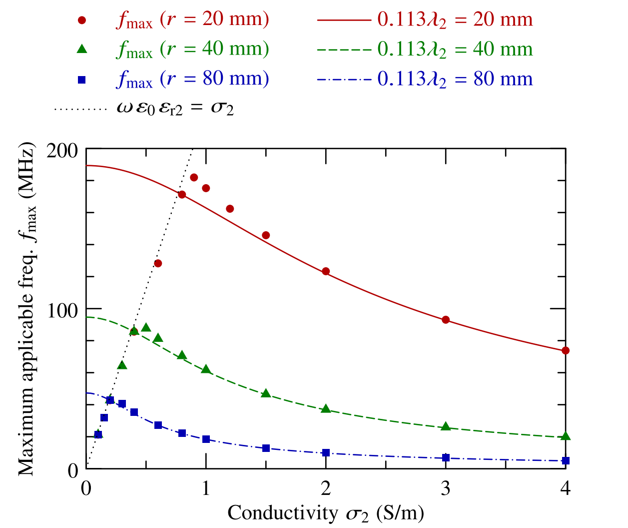

Fig. 5. $f_{\max}$ versus σ_2 at $r = 20$, 40, and 80 mm ($\varepsilon_{\mathrm{r1}} = 1$ and $L = 64$).

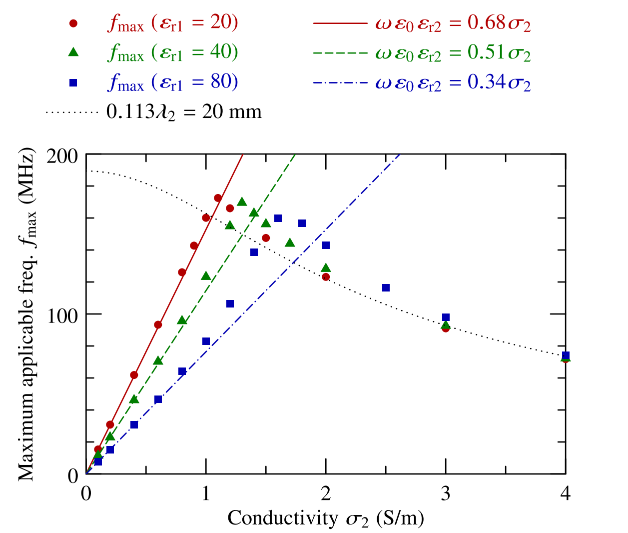

Fig. 6. $f_{\max}$ versus σ_2 at $\varepsilon_{\mathrm{r1}} = 20$, 40, and 80 ($r = 20$ mm and $L = 64$).

In Fig. 5, the circular, triangular, and square markers represent the dependence of $f_{\max}$ on σ_2 at $r = 20$, 40, and 80 mm, respectively ($\varepsilon_{\mathrm{r1}} = 1$ and $L = 64$). In addition, the solid, dashed, and chained lines represent the frequencies satisfying $0.113\lambda_2 = 20$, 40, and 80 mm, respectively (λ_2 is the wavelength in the lossy dielectric), whereas the dotted line represents the frequency satisfying $\omega\varepsilon_0\varepsilon_{\mathrm{r2}} = \sigma_2$ (ε_0 is vacuum permittivity). The result shows that $f_{\max}$ approximately coincides with the lower of the frequencies satisfying $0.113\lambda_2 = r$ and $\omega\varepsilon_0\varepsilon_{\mathrm{r2}} = \sigma_2$. In other words, the applicable frequency of the IDEM is limited by both the electrical size of the lossless dielectric and the radius of convergence in (9), as expected.

Then, the effect of the relative permittivity $\varepsilon_{\mathrm{r1}}$ of lossless dielectric on $f_{\max}$ is evaluated. In Fig. 6, the circular, triangular, and square markers represent the dependence of $f_{\max}$ on σ_2 at $\varepsilon_{\mathrm{r1}} = 20$, 40, and 80, respectively ($r = 20$ mm and $L = 64$). In addition, the solid, dashed, and chained lines

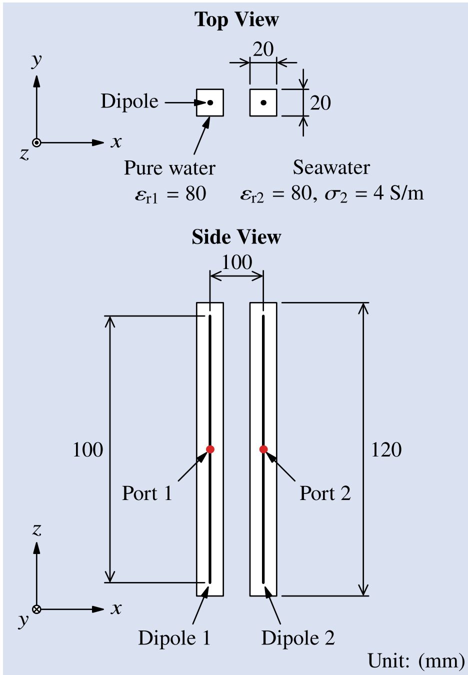

Fig. 7. Undersea dipole antennas with pure water covers.

represent the frequencies satisfying $\omega\varepsilon_0\varepsilon_{r2} = 0.68\sigma_2$, $0.51\sigma_2$, and $0.34\sigma_2$, respectively, whereas the dotted line represents the frequency satisfying $0.113\lambda_2 = 20$ mm. The result shows that the slope of the line approximating $f_{\max}$ at small σ_2 decreases with increasing ε_{r1}. Moreover, an additional parameter study found that the slope satisfies the following empirical formula:

$$\omega\varepsilon_0(\alpha\varepsilon_{r1} + \varepsilon_{r2}) \simeq \sigma_2 \tag{22}$$

where α is a constant that depends mainly on the shape of the lossless dielectric. For example, $\alpha \simeq 1.96$ and 4.3 if the lossless dielectric is spherical and cubic, respectively. At this stage, the reason why this empirical formula holds is unclear and will need to be investigated further in the future.

IV. Circuit Modeling of Undersea Antennas

In this section, to demonstrate the applicability of the IDEM, circuit modeling of near-field coupled undersea dipole and loop antennas enclosed in pure water covers is performed, and the effects of the covers on the circuit parameters are clarified. It is emphasized that the geometries of these antennas are basic, whereas those of the covers are arbitrary.

A. Undersea Dipole Antennas

As shown in Fig. 7, straight dipoles 1 and 2 that are composed of perfectly conducting wires of radius 0.4 mm are separately enclosed in pure water covers ($\varepsilon_{r1} = 80$). Although actual pure water has a conductivity of approximately 0.2 mS/m (distilled water) to 20 mS/m (drinking water) [8], its conductivity is assumed to be zero because the degree of conductivity has little effect on results. The dipoles and covers are mirror symmetric about the xy, xz, and yz planes passing through the central point on the line segment between the ports 1 and 2. The outside of the covers is assumed to be seawater ($\varepsilon_{r2} = 80$ and $\sigma_2 = 4$ S/m). Practically, the pure water and seawater should be separated by a solid material such as a resin. However, such a separating material is not considered for simplicity. Since the dipoles and covers fit into a sphere whose radius is approximately 114 mm, the IDEM applies to frequencies up to approximately 2.43 MHz, according to the discussion in Section III.

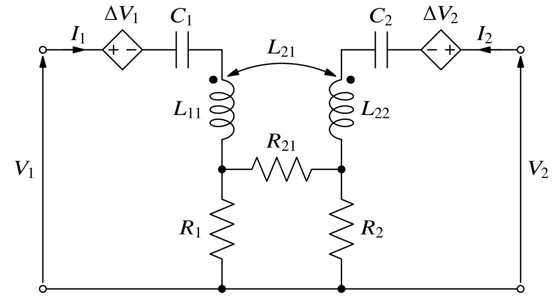

Fig. 8. Circuit model of the undersea dipole antennas.

In the usual MoM, current distributions of antennas are discretized into multiple basis functions. However, this leads to an increase in the size of the resulting circuit model and thus spoils its advantages. Therefore, the current distributions of dipoles 1 and 2 are approximated only by piecewise linear basis functions $\boldsymbol{F}_1$ and $\boldsymbol{F}_2$, respectively. The numbers of the star and loop basis functions on the surfaces of the pure water covers are $N_\star = 1406$ and $N_\circ = 1410$, respectively. The difference in the resulting circuit parameters when the number of basis functions is increased by four times was confirmed to be less than 0.16%.

The self- and mutual impedances between ports 1 and 2 are approximated by a Laurent series of finite order as follows:

$$Z_{ij} \simeq s^{-1}Z_{ij}^{(-1)} + Z_{ij}^{(0)} + sZ_{ij}^{(1)} + s^{3/2}Z_{ij}^{(3/2)} \tag{23}$$

where $Z_{21}^{(-1)} = 0$ because no electrostatic field can exist in the seawater, which separates $\boldsymbol{F}_1$ and $\boldsymbol{F}_2$. In addition, $Z_{ij}^{(0)}$ and $Z_{ij}^{(3/2)}$ consist only of the scattering components, where the former is caused by the steady-state currents in seawater and the latter represents the radiation loss of equivalent electric dipole moments in an extended sense, as discussed later.

Fig. 8 shows the circuit model of the undersea dipole antennas, where V_i and I_i are the voltage and current of port i, respectively ($i = 1, 2$). The capacitances represent the self-impedance components proportional to s^{-1}, that is,

$$C_i = 1/Z_{ii}^{(-1)}. \tag{24}$$

The resistances represent the impedance components independent of s, that is,

$$\left.\begin{aligned} R_1 &= \frac{Z_{11}^{(0)}Z_{22}^{(0)} - Z_{21}^{(0)2}}{Z_{22}^{(0)} - Z_{21}^{(0)}}, \quad R_2 = \frac{Z_{11}^{(0)}Z_{22}^{(0)} - Z_{21}^{(0)2}}{Z_{11}^{(0)} - Z_{21}^{(0)}} \\ R_{21} &= \frac{Z_{11}^{(0)}Z_{22}^{(0)}}{Z_{21}^{(0)}} - Z_{21}^{(0)} \end{aligned}\right\}. \tag{25}$$

The self- and mutual inductances correspond to the impedance components proportional to s, that is,

$$L_{ij} = Z_{ij}^{(1)}. \tag{26}$$

The dependent voltage sources represent the voltage drops caused by the impedance components proportional to $s^{3/2}$, that is,

$$\Delta V_i = \sum_{j=1}^{2} s^{3/2} Z_{ij}^{(3/2)} I_j. \tag{27}$$

Table I summarizes the circuit parameters of the undersea dipole antennas with and without the pure water covers. The resistances without the covers can be obtained by substituting

$$Z_{ij}^{(0)} = \frac{1}{\sigma_2} X(\boldsymbol{F}_i, \boldsymbol{F}_j, -1) \tag{28}$$

into (25). The expression in (28) corresponds to the fact that the near-field produced by an electric dipole in lossy dielectrics can be approximated as inversely proportional to conductivity and independent of frequency [34]. On the other hand, the other parameters without the covers can be expressed as follows:

$$L_{ij} = \mu_0 X(\boldsymbol{F}_i, \boldsymbol{F}_j, 1) - \frac{\varepsilon_0 \varepsilon_{r2}}{\sigma_2^2} X(\boldsymbol{F}_i, \boldsymbol{F}_j, -1) \tag{29}$$

$$Z_{ij}^{(3/2)} = \mu_0^{3/2} \sigma_2^{1/2} X(\boldsymbol{F}_i, \boldsymbol{F}_j, 2) \tag{30}$$

where μ_0 is vacuum permeability. These parameters without the covers were obtained analytically. Although (29) is the expression for those without the covers, it implies that the self- and mutual inductances of the undersea dipole antennas with the covers depend not only on permeability but also permittivity and conductivity. In addition, $X(\boldsymbol{F}_i, \boldsymbol{F}_j, 2)$ in (30) can be expressed as follows [17]:

$$X(\boldsymbol{F}_i, \boldsymbol{F}_j, 2) = -\frac{1}{6\pi} \left(\int_S \boldsymbol{F}_i \, dS \right) \cdot \left(\int_S \boldsymbol{F}_j \, dS \right) \tag{31}$$

where S is the support of $\boldsymbol{F}_i$ and $\boldsymbol{F}_j$, and each integral represents an electric dipole moment. Approximating $\zeta_2 \simeq \sqrt{s\mu_0/\sigma_2}$ and $\gamma_2 \simeq \sqrt{s\mu_0\sigma_2}$, and integrating the far-field Poynting vector caused by the equivalent electric dipole moments over the spherical surface of radius r yields

$$P_r = \frac{\omega^{3/2} \mu_0^{3/2} \sigma_2^{1/2} e^{-2\alpha_2 r}}{2^{1/2} 6\pi} \times \sum_{i=1}^{2} \sum_{j=1}^{2} I_i^* I_j \left(\int_S \boldsymbol{F}_i \, dS \right) \cdot \left(\int_S \boldsymbol{F}_j \, dS \right) \tag{32}$$

which is always positive and equal to the power dissipated by the impedance components $Z_{ij}^{(3/2)}$ in (30) multiplied by the attenuation factor $e^{-2\alpha_2 r}$, where $\alpha_2 = \Re(\gamma_2)$. Therefore, $Z_{ij}^{(3/2)}$ can be regarded as radiation resistances in an extended sense. According to Table I, the resistances $R_1 = R_2$ and R_{21} are significantly reduced by approximately 60% and 91%, respectively, by the presence of the covers. On the other hand, the self-inductances $L_{11} = L_{22}$ are reduced by approximately 2.3% and the mutual inductance L_{21} is increased by approximately 6.7%. Although these changes are not very significant, they are to be expected from (29). Meanwhile, the relation $Z_{11}^{(3/2)} \simeq Z_{21}^{(3/2)}$ holds regardless of the presence or absence of the covers, which can be predicted from (31), that is, the equivalent electric dipole moments of $\boldsymbol{F}_1$ and $\boldsymbol{F}_2$ are parallel.

TABLE I

CIRCUIT PARAMETERS OF UNDERSEA DIPOLE ANTENNAS

	w/ covers	w/o covers
$C_1 = C_2$ (F)	7.003×10^{-11}	∞
$R_1 = R_2$ (Ω)	1.599	3.959
R_{21} (Ω)	3.321	3.607×10
$L_{11} = L_{22}$ (H)	6.802×10^{-8}	6.960×10^{-8}
L_{21} (H)	1.268×10^{-8}	1.189×10^{-8}
$Z_{11}^{(3/2)} = Z_{22}^{(3/2)}$ ($\Omega \cdot s^{3/2}$)	-1.537×10^{-12}	-1.495×10^{-12}
$Z_{21}^{(3/2)}$ ($\Omega \cdot s^{3/2}$)	-1.537×10^{-12}	-1.495×10^{-12}

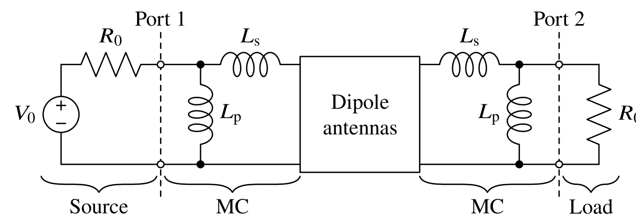

Fig. 9. Dipole antennas with a power source, a load, and MCs.

Since the heat loss due to seawater causes an increase in its conductivity, the effect of the conductivity on the circuit parameters is discussed briefly. As described earlier, seawater behaves as a perfect conductor for electrostatic fields, so the capacitances are independent of the conductivity. On the other hand, the other parameters depend on the conductivity as expected from (28)–(30), that is, $Z_{ij}^{(0)}$ and $Z_{ij}^{(3/2)}$ are proportional to σ_2^{-1} and $\sigma_2^{1/2}$, respectively, whereas $Z_{ij}^{(1)}$ converges to a constant value when σ_2 becomes somewhat large.

Then, the dipole antennas with a power source, a load, and matching circuits (MCs), which is shown in Fig. 9, are evaluated. The parallel inductor of $L_p = 2.993$ μH and the series inductor of $L_s = 2.245$ mH are selected so that the antennas are matched with the source and load of $R_0 = 50$ Ω at 400 kHz.

Fig. 10 shows the frequency dependences of the reflection coefficient $|S_{11}|$ and transmission coefficient $|S_{21}|$ of the undersea dipole antennas with the pure water covers, where the results by the circuit model, full-wave MoM (FW-MoM), and finite-difference time-domain (FDTD) method [35] are compared. In the FW-MoM, the currents of the wires are expanded into 30 piecewise linear basis functions, whereas the basis functions on the surface of the covers are the same as those in the IDEM. In the FDTD method, the cell size is 2 mm inside the covers and increases up to 10 mm away from the covers. The dimensions of the computational domain are 0.5 × 0.5 × 0.5 m. The absorbing boundary condition is the perfectly matched layer of 64 layers. The results by the FW-MoM and FDTD results are in good agreement, in general. As the discrepancy between these resonant frequencies is only 0.038%, they can be regarded as reference solutions. On the other hand, the result of the circuit model shows that the peak value of $|S_{21}|$ is approximately the same as those by the other methods, but the resonant frequency is approximately 0.28% higher than that by the FW-MoM. This discrepancy is

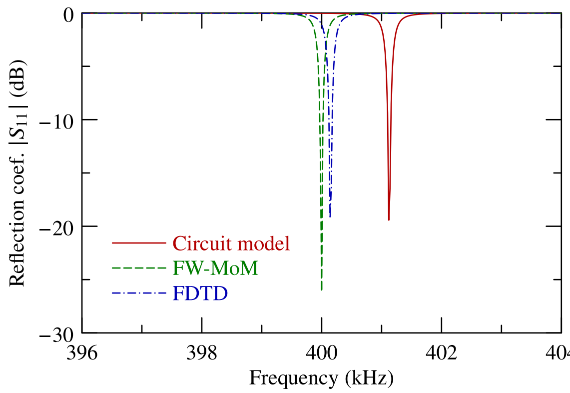

(a)

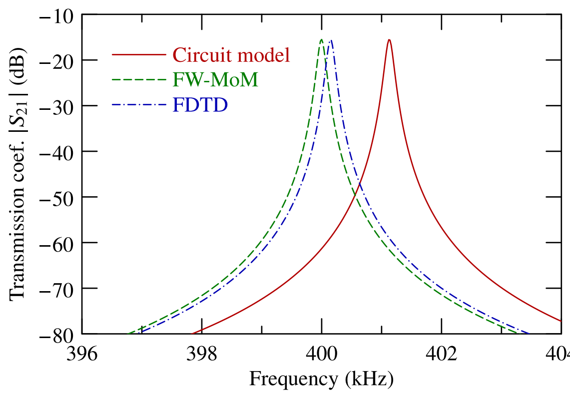

(b)

Fig. 10. Frequency dependences of (a) reflection coefficient $|S_{11}|$ and (b) transmission coefficient $|S_{21}|$ of the undersea dipole antennas with the pure water covers.

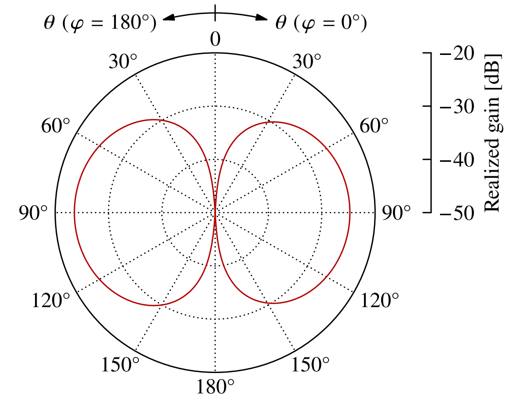

Fig. 11. Realized gain of the undersea dipole antennas with the pure water covers (E_θ component at 400 kHz, calculated by the FW-MoM).

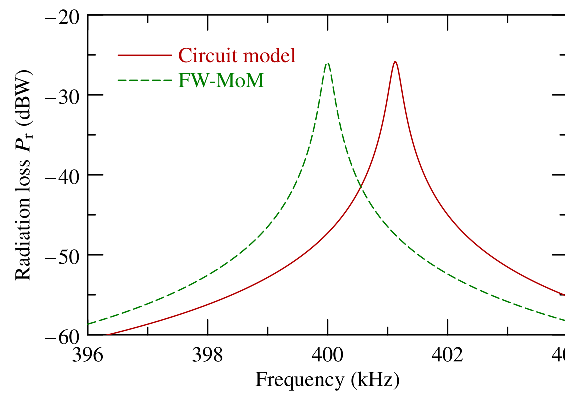

Fig. 12. Frequency dependence of the radiation loss of the undersea dipole antennas with the pure water covers, where the results by the circuit model and FW-MoM are based on (33) and (35), respectively.

because the current of each dipole is approximated by a single piecewise linear basis function to derive the circuit model. Although this discrepancy can be resolved by increasing the number of basis functions representing the current distributions of the wires, improving the accuracy while keeping the size of the circuit model small is a future challenge. In addition, although not shown in the figure, it has been confirmed that the resulting S-parameters hardly change even if the impedance components $Z_{ij}^{(3/2)}$ are ignored.

As already shown theoretically, in the absence of the pure water covers, the power dissipated by the impedance components $Z_{ij}^{(3/2)}$ multiplied by the attenuation factor $e^{-2\alpha_2 r}$ is equivalent to the radiation loss in the extended sense (integral value of the far-field Poynting vector). To verify whether this relationship holds in the presence of the pure water covers, the power dissipated by the impedance component $Z_{ij}^{(3/2)}$ is compared with the radiation loss calculated by the FW-MoM. The radiation loss P_r in the circuit model is obtained as follows:

$$P_r = \sum_{i=1}^{2}\sum_{j=1}^{2} \Re\left[s^{3/2} Z_{ij}^{(3/2)} I_i^* I_j\right]. \tag{33}$$

Note that the attenuation factor is excluded here, and the same is applied to the subsequent evaluations. On the other hand, the radiation loss in the FW-MoM is obtained by integrating the far-field Poynting vector. For reference, Fig. 11 shows the realized gain (E_θ component at 400 kHz) of the undersea dipole antennas with the pure water covers. Note that its definition is extended for antennas in a conductive space as in [37], that is,

$$G_\psi = \lim_{r\to\infty} \frac{4\pi r^2 \Re\left(\zeta_2^{-1}\right)|E_\psi|^2}{e^{-2\alpha_2 r} P_{\rm ava}}, \quad \psi = \theta, \varphi. \tag{34}$$

Note that the one in [37] is an absolute gain with respect to the input power, whereas the one defined by (34) is a realized gain with respect to the available power $P_{\rm ava}$. By integrating the far-field Poynting vector with such directivity over the spherical surface of radius r, and then dividing it by the attenuation factor $e^{-2\alpha_2 r}$, the radiation loss P_r in the FW-MoM can be obtained as follows:

$$P_r = \lim_{r\to\infty} \frac{r^2 \Re\left(\zeta_2^{-1}\right)}{e^{-2\alpha_2 r}} \int_0^{2\pi}\int_0^{\pi} |\boldsymbol{E}|^2 \sin\theta \, d\theta \, d\varphi. \tag{35}$$

Fig. 12 shows the frequency dependence of the radiation loss P_r of the undersea dipole antennas with the pure water covers calculated by the circuit model and FW-MoM, where the available power of the power source is assumed to be $P_{\rm ava} = 1$ W. As with the S-parameters, there is a discrepancy in the resonant frequency, but the peak values and general trends are similar, indicating that the equivalence of both holds even in the presence of the pure water covers.

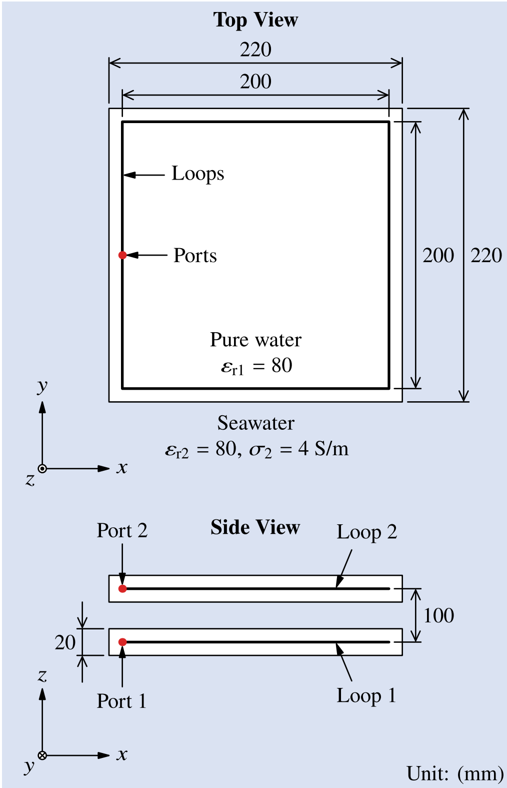

Fig. 13. Undersea loop antennas with pure water covers.

B. Undersea Loop Antennas

As shown in Fig. 13, square loops 1 and 2 are composed of perfectly conducting wires of radius 0.4 mm are separately enclosed in pure water covers ($\varepsilon_{r1} = 80$) whose conductivity is assumed to be zero. The loops and covers are mirror symmetric about the xy and xz planes passing through the central point on the line segment between the loop centers. The outside of the covers is assumed to be seawater ($\varepsilon_{r2} = 80$ and $\sigma_2 = 4$ S/m). As in the case of the dipole antennas, a solid material separating seawater and pure water is not considered for simplicity. Since the loops and covers fit into a sphere whose radius is approximately 158 mm, the IDEM applies to frequencies up to approximately 1.27 MHz, according to the discussion in Section III.

The current distributions of loops 1 and 2 are expressed by filamentary basis functions $\boldsymbol{F}_1$ and $\boldsymbol{F}_2$ that are uniform along the wire axes, respectively. The numbers of the star and loop basis functions on the surfaces of the pure water covers are $N_\star = 2158$ and $N_\circ = 2162$, respectively. The difference in the resulting circuit parameters when the number of basis functions is increased by four times was confirmed to be less than 0.025%.

Since $\boldsymbol{F}_1$ and $\boldsymbol{F}_2$ are assumed to be solenoidal, that is, $Z_{ij}^{(-1)} = Z_{ij}^{(0)} = Z_{ij}^{(3/2)} = 0$, the self- and mutual impedances between ports 1 and 2 are approximated by a Taylor series of finite order as follows:

$$Z_{ij} \simeq sZ_{ij}^{(1)} + s^2 Z_{ij}^{(2)} + s^{5/2} Z_{ij}^{(5/2)} \tag{36}$$

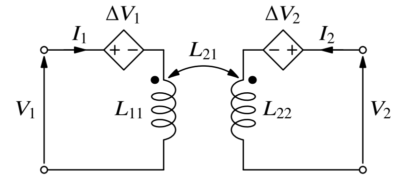

Fig. 14. Circuit model of the undersea loop antennas.

TABLE II
CIRCUIT PARAMETERS OF UNDERSEA LOOP ANTENNAS

	w/ covers	w/o covers
$L_{11} = L_{22}$ (H)	8.743×10^{-7}	8.708×10^{-7}
L_{21} (H)	1.670×10^{-7}	1.654×10^{-7}
$Z_{11}^{(2)} = Z_{22}^{(2)}$ $(\Omega\cdot s^2)$	-5.287×10^{-15}	-5.978×10^{-15}
$Z_{21}^{(2)}$ $(\Omega\cdot s^2)$	-4.992×10^{-15}	-5.506×10^{-15}
$Z_{11}^{(5/2)} = Z_{22}^{(5/2)}$ $(\Omega\cdot s^{5/2})$	1.214×10^{-18}	1.202×10^{-18}
$Z_{21}^{(5/2)}$ $(\Omega\cdot s^{5/2})$	1.214×10^{-18}	1.202×10^{-18}

where $Z_{ij}^{(2)}$ and $Z_{ij}^{(5/2)}$ consist only of the scattering components, the former of which is obtained as follows:

$$Z_{ij}^{\mathrm{sc}(2)} = \begin{bmatrix} \mathbf{Z}_{i\circ}^{(1)} & \mathbf{U}_{i\star}^{(0)} \end{bmatrix} \begin{bmatrix} \mathbf{I}_\circ^{(1)} \\ \mathbf{V}_\star^{(2)} \end{bmatrix} \tag{37}$$

where $\mathbf{I}_\circ^{(1)}$ corresponds to the eddy current caused by the magnetostatic field due to $I_j \boldsymbol{F}_j$ and Faraday's law. Note that [36] has also shown that eddy currents are linearly proportional to the frequency. According to (37), $\mathbf{I}_\circ^{(1)}$ and $\boldsymbol{F}_i$ are coupled through mutual inductances $\mathbf{Z}_{i\circ}^{(1)}$, resulting in $Z_{ij}^{\mathrm{sc}(2)}$. This interpretation theoretically supports the discussion in [16]. On the other hand, $Z_{ij}^{(5/2)}$ represents the radiation loss of an equivalent magnetic dipole moment in an extended sense, as discussed later.

Fig. 14 shows the circuit model of the undersea loop antennas, where V_i and I_i are the voltage and current of port i, respectively ($i = 1, 2$). The self- and mutual inductances correspond to the impedance components proportional to s, as in (26). The dependent voltage sources represent the voltage drops caused by the impedance components proportional to s^2 and $s^{5/2}$, that is,

$$\Delta V_i = \sum_{j=1}^{2} \left[s^2 Z_{ij}^{(2)} + s^{5/2} Z_{ij}^{(5/2)} \right] I_j \tag{38}$$

where the contribution of the quadratic components can also be approximated only by passive elements [19].

Table II summarizes the circuit parameters of the undersea loop antennas with and without the pure water covers, the latter of which can be expressed as follows:

$$L_{ij} = \mu_0 X(\boldsymbol{F}_i, \boldsymbol{F}_j, 1) \tag{39}$$

$$Z_{ij}^{(2)} = \mu_0^2 \sigma_2 X(\boldsymbol{F}_i, \boldsymbol{F}_j, 3) \tag{40}$$

$$Z_{ij}^{(5/2)} = \mu_0^{5/2} \sigma_2^{3/2} X(\boldsymbol{F}_i, \boldsymbol{F}_j, 4). \tag{41}$$

These parameters without the covers were obtained analytically. Unlike (29), the expression in (39) does not contain the term dependent on permittivity and conductivity because

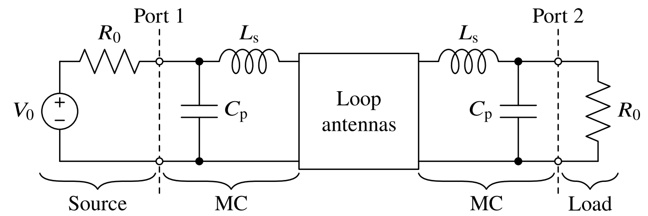

Fig. 15. Loop antennas with a source, a load, and MCs.

$\boldsymbol{F}_1$ and $\boldsymbol{F}_2$ are solenoidal. Therefore, it is identical to the self-/mutual inductance in free space. In addition, as proved in Appendix B, since $\boldsymbol{F}_i$ and $\boldsymbol{F}_j$ are solenoidal, $X(\boldsymbol{F}_i, \boldsymbol{F}_j, 4)$ in (41) can be expressed as follows:

$$X(\boldsymbol{F}_i, \boldsymbol{F}_j, 4) = \frac{1}{6\pi}\left(\int_S \frac{\boldsymbol{r}\times\boldsymbol{F}_i}{2} dS\right) \cdot \left(\int_S \frac{\boldsymbol{r}\times\boldsymbol{F}_j}{2} dS\right) \tag{42}$$

where $\boldsymbol{r}$ is the position vector and each integral represents a magnetic dipole moment. Approximating $\zeta_2 \simeq \sqrt{s\mu_0/\sigma_2}$ and $\gamma_2 \simeq \sqrt{s\mu_0\sigma_2}$, and integrating the far-field Poynting vector caused by the equivalent magnetic dipole moments over the spherical surface of radius r yields

$$P_r = \frac{\omega^{5/2}\mu_0^{5/2}\sigma_2^{3/2}e^{-2\alpha_2 r}}{2^{1/2}6\pi} \times \sum_{i=1}^{2}\sum_{j=1}^{2} I_i^* I_j \left(\int_S \frac{\boldsymbol{r}\times\boldsymbol{F}_i}{2} dS\right) \cdot \left(\int_S \frac{\boldsymbol{r}\times\boldsymbol{F}_j}{2} dS\right) \tag{43}$$

which is always positive. On the other hand, the power due to the impedance components $Z_{ij}^{(5/2)}$ in (41) multiplied by the attenuation factor $e^{-2\alpha_2 r}$ is equal in magnitude to P_r in (43), but its sign is opposite, that is, it contributes negatively to the total loss. Thus, the physical interpretation of $Z_{ij}^{(5/2)}$ is complicated, but the discussion proceeds as if $Z_{ij}^{(5/2)}$ is related to the radiation loss, as in the case of the dipole antennas in Section IV-A. According to Table II, the self- and mutual inductances with the covers are approximately the same as those without the covers. In other words, it is supported that the self- and mutual inductances between undersea loop antennas can be identified by Neumann's formula in free space, regardless of the presence or absence of pure water covers. In contrast, the quadratic impedance components are reduced by the presence of the pure water covers, which means the reduction of the eddy current losses. Meanwhile, the relation $Z_{11}^{(5/2)} \simeq Z_{21}^{(5/2)}$ holds regardless of the presence or absence of the covers, which can be predicted from (42), that is, the equivalent magnetic dipole moments of $\boldsymbol{F}_1$ and $\boldsymbol{F}_2$ are parallel.

In addition, whereas the inductances are independent of the conductivity as described earlier, $Z_{ij}^{(2)}$ and $Z_{ij}^{(5/2)}$ are proportional to σ_2 and $\sigma_2^{3/2}$, respectively, as expected from (40) and (41).

Then, the loop antennas with a power source, a load, and MCs, which are shown in Fig. 15, are evaluated. The parallel capacitor of $C_p = 142.1$ nF and the series inductor of $L_s = 39.05$ nH are selected so that the antennas are matched with the source and load of $R_0 = 50\ \Omega$ at 400 kHz.

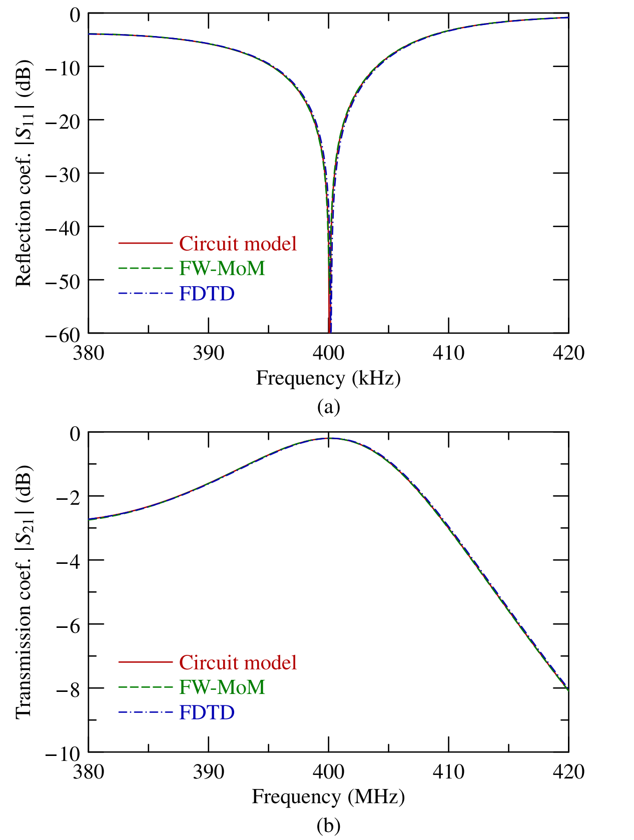

Fig. 16. Frequency dependences of (a) reflection coefficient $|S_{11}|$ and (b) transmission coefficient $|S_{21}|$ of the undersea loop antennas with the pure water covers.

Fig. 16 shows the frequency dependences of the reflection coefficient $|S_{11}|$ and transmission coefficient $|S_{21}|$ of the undersea loop antennas with the pure water covers, where the results by the circuit model, FW-MoM, and FDTD method are compared. In the FW-MoM, the currents of the wires are expressed by 126 piecewise linear basis functions in addition to the uniform loop basis functions, whereas the basis functions on the surface of the covers are the same as those in the IDEM. The computational conditions for the FDTD method are similar to those in the case of the undersea dipole antennas. The good agreement between the results of the three methods indicates their validity. In particular, the assumption of uniform current distribution for each loop in deriving the circuit model is considered to be a good enough approximation. In addition, although not shown in the figure, it has been confirmed that the resulting S-parameters hardly change even if the impedance components $Z_{ij}^{(5/2)}$ are ignored.

As already shown theoretically, in the absence of the pure water covers, the power due to the impedance components $Z_{ij}^{(5/2)}$ multiplied by the attenuation factor $e^{-2\alpha_2 r}$ is equal in magnitude and opposite in sign to the radiation loss in the extended sense. To verify how this relationship holds in the presence of the pure water covers, the power due to the impedance components $Z_{ij}^{(5/2)}$ is compared with the radiation

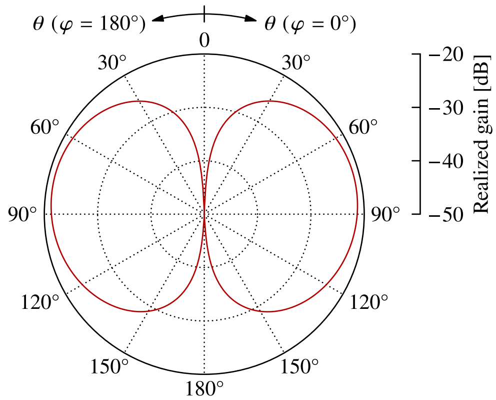

Fig. 17. Realized gain of the undersea loop antennas with the pure water covers (E_φ component at 400 kHz, calculated by the FW-MoM).

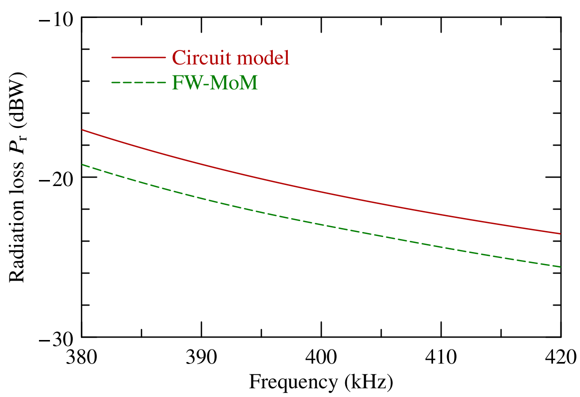

Fig. 18. Frequency dependence of the radiation loss of the undersea loop antennas with the pure water covers, where the results by the circuit model and FW-MoM are based on (44) and (35), respectively.

loss calculated by the FW-MoM. The radiation loss P_r in the circuit model is obtained as follows:

$$P_\mathrm{r} = -\sum_{i=1}^{2}\sum_{j=1}^{2} \Re\left[s^{5/2} Z_{ij}^{(5/2)} I_i^* I_j\right]. \tag{44}$$

On the other hand, the radiation loss in the FW-MoM is obtained by integrating the far-field Poynting vector based on (35), as in the case of the dipole antennas. For reference, Fig. 17 shows the realized gain (E_φ component at 400 kHz) of the undersea loop antennas with the pure water covers. Fig. 18 shows the frequency dependence of the radiation loss P_r of the undersea loop antennas with the pure water covers calculated by the circuit model and FW-MoM, where the available power of the power source is assumed to be $P_\mathrm{ava} = 1$ W. There is a difference of approximately 2 dB in the radiation loss obtained by the two methods. Although the cause of this difference is not clear, the presence of the pure water covers, which were not assumed in the aforementioned theoretical discussion, is one possible reason for the difference. In fact, additional numerical calculations have verified that the radiation losses obtained by the two methods are identical if no pure water cover and uniform current distributions are assumed in both the circuit model and FW-MoM. Nevertheless, the trends of the frequency dependence in Fig. 18 are consistent, suggesting that the radiation losses by the two methods are related to each other even in the presence of the pure water covers.

C. Computational Cost

The memory usage and execution time for the IDEM are discussed in comparison to the FW-MoM. The comparison is based on the case of the undersea loop antennas described in Section IV-B. Both methods were implemented with double-precision data and parallelized with OpenMP. The execution times were measured on a workstation with an Apple M1 Ultra system-on-a-chip (3.2 GHz $\times$ 16 cores + 2.0 GHz $\times$ 4 cores).

The memory usage for storing the matrix elements in the FW-MoM is approximately 1.23 GB, whereas that in the IDEM is approximately 2.09 GB. Thus, at least in this condition, the IDEM requires more memory than the FW-MoM. However, the advantage of the IDEM is its much shorter execution time, as described below.

The execution time in the FW-MoM was approximately 17.5 s per frequency (13.9 s for matrix generation and 3.64 s for LU factorization). On the other hand, the execution time for obtaining the circuit parameters in the IDEM was approximately 22.5 s [21.8 s for matrix generation and 0.64 s for solving (13), (14), and (19)], which is longer than the execution time per frequency in the FW-MoM. However, the resulting circuit model requires only approximately 5.88 μs per frequency during the frequency sweep. Therefore, when obtaining results at more than a few frequencies, the IDEM requires much less execution time than the FW-MoM, which demonstrates the advantage of the circuit modeling by the IDEM.

V. Conclusion

In this study, the IEM was further extended to be applied to circuit modeling of near-field coupled undersea antennas. The extended method is called the IDEM because of its feature that the coefficient matrices derived by the MoM are first expanded with respect to the propagation constants, and then further expanded with respect to the complex angular frequency.

The IDEM can be applied to frequencies where the lossless dielectric is electrically small and the loss tangent of the lossy dielectric is greater than a certain value. For example, if the lossless dielectric is spherical, its radius must be less than 0.113 times the wavelength in the surrounding lossy dielectric. If the permittivity of the lossless dielectric is much smaller than that of the lossy dielectric, the loss tangent of the lossy dielectric must be greater than 1. As the permittivity of the lossless dielectric increases, the loss tangent of the lossy dielectric must become larger.

The IDEM was applied to undersea dipole and loop antennas with pure water covers, and their circuit models were obtained. The circuit model of the undersea dipole antennas consists of capacitors, resistors, inductors, and impedance components proportional to $s^{3/2}$, where the resistances are greatly reduced by the presence of the water covers. In addition, the power dissipated by the impedance components proportional to $s^{3/2}$ corresponds to the radiation loss in the extended sense (power obtained by integrating the far-field Poynting vector on a sphere of radius r and dividing it by the attenuation factor $e^{-2\alpha_2 r}$).

On the other hand, the circuit model of the undersea loop antennas consists of inductors and impedance components proportional to s^2 and $s^{5/2}$. Among them, the inductance values are hardly affected by the pure water covers and can be identified by Neumann's formula in free space. In addition, the impedance components proportional to s^2 represent the eddy current loss in the seawater, which supports the discussion in the previous study. Furthermore, the power due to the impedance components proportional to $s^{5/2}$ is negative, and its absolute value is approximately 2 dB larger than the radiation loss in the extended sense, but their trends of the frequency dependence are consistent, suggesting that they are related to each other.

These circuit models provide a reasonable approximation of the S-parameters between antennas with MCs. However, in the case of the dipole antennas, the current distribution of each element is approximated by a single basis function, which causes errors that need to be reduced in the future.

In addition, since the computational cost of the frequency sweeping using the circuit model is negligible, the IDEM requires much less execution time than that in the FW-MoM, which demonstrates the advantage of the circuit modeling by the IDEM.

Appendix A
Elements of Expanded Matrices in (10)

If k is even, then the (i, j)th elements of $\bar{\mathbf{Z}}_{\tau\upsilon}^{(k/2)}$, $\bar{\mathbf{Y}}_{\tau\upsilon}^{(k/2)}$, and $\bar{\mathbf{U}}_{\tau\upsilon}^{(k/2)}$ in (10) are expressed as follows:

$$\begin{aligned}\left[\bar{\mathbf{Z}}_{\tau\upsilon}^{(k/2)}\right]_{ij} &= \sqrt{\frac{\mu_1}{\varepsilon_1}}(\varepsilon_1\mu_1)^{k/4}X\left(\boldsymbol{F}_i^{\tau}, \boldsymbol{F}_j^{\upsilon}, k/2\right)\\ &\quad + \frac{1}{\sigma_2}\sum_{l=0}^{k/2}\binom{l-1}{k/2-l}\left(\frac{\varepsilon_2}{\sigma_2}\right)^{k/2-l}\\ &\quad \times (\mu_2\sigma_2)^l X\left(\boldsymbol{F}_i^{\tau}, \boldsymbol{F}_j^{\upsilon}, 2\,l-1\right)\end{aligned} \tag{45}$$

$$\begin{aligned}\left[\bar{\mathbf{Y}}_{\tau\upsilon}^{(k/2)}\right]_{ij} &= \sqrt{\frac{\varepsilon_1}{\mu_1}}(\varepsilon_1\mu_1)^{k/4}X\left(\boldsymbol{F}_i^{\tau}, \boldsymbol{F}_j^{\upsilon}, k/2\right)\\ &\quad + \sigma_2\sum_{l=0}^{k/2+1}\binom{l}{k/2+1-l}\left(\frac{\varepsilon_2}{\sigma_2}\right)^{k/2+1-l}\\ &\quad \times (\mu_2\sigma_2)^{l-1} X\left(\boldsymbol{F}_i^{\tau}, \boldsymbol{F}_j^{\upsilon}, 2\,l-1\right)\end{aligned} \tag{46}$$

$$\begin{aligned}\left[\bar{\mathbf{U}}_{\tau\upsilon}^{(k/2)}\right]_{ij} &= (\varepsilon_1\mu_1)^{k/4}W\left(\boldsymbol{F}_i^{\tau}, \boldsymbol{F}_j^{\upsilon}, k/2\right)\\ &\quad + \sum_{l=0}^{k/2}\binom{l}{k/2-l}\left(\frac{\varepsilon_2}{\sigma_2}\right)^{k/2-l}\\ &\quad \times (\mu_2\sigma_2)^l W\left(\boldsymbol{F}_i^{\tau}, \boldsymbol{F}_j^{\upsilon}, 2\,l\right).\end{aligned} \tag{47}$$

If k is odd, then

$$\begin{aligned}\left[\bar{\mathbf{Z}}_{\tau\upsilon}^{(k/2)}\right]_{ij} &= \frac{1}{\sigma_2}\sum_{l=1}^{(k-1)/2}\binom{l-1/2}{(k-1)/2-l}\left(\frac{\varepsilon_2}{\sigma_2}\right)^{(k-1)/2-l}\\ &\quad \times (\mu_2\sigma_2)^{l+1/2} X\left(\boldsymbol{F}_i^{\tau}, \boldsymbol{F}_j^{\upsilon}, 2\,l\right)\end{aligned} \tag{48}$$

$$\begin{aligned}\left[\bar{\mathbf{Y}}_{\tau\upsilon}^{(k/2)}\right]_{ij} &= \sigma_2\sum_{l=1}^{(k+1)/2}\binom{l+1/2}{(k+1)/2-l}\left(\frac{\varepsilon_2}{\sigma_2}\right)^{(k+1)/2-l}\\ &\quad \times (\mu_2\sigma_2)^{l-1/2} X\left(\boldsymbol{F}_i^{\tau}, \boldsymbol{F}_j^{\upsilon}, 2\,l\right)\end{aligned} \tag{49}$$

$$\begin{aligned}\left[\bar{\mathbf{U}}_{\tau\upsilon}^{(k/2)}\right]_{ij} &= \sum_{l=1}^{(k-1)/2}\binom{l+1/2}{(k-1)/2-l}\left(\frac{\varepsilon_2}{\sigma_2}\right)^{(k-1)/2-l}\\ &\quad \times (\mu_2\sigma_2)^{l+1/2} W\left(\boldsymbol{F}_i^{\tau}, \boldsymbol{F}_j^{\upsilon}, 2\,l+1\right).\end{aligned} \tag{50}$$

Appendix B
Proof of (42)

According to (6) in [21], if $\boldsymbol{F}_i$ and $\boldsymbol{F}_j$ are solenoidal, then $X(\boldsymbol{F}_i, \boldsymbol{F}_j, 4)$ is expressed as follows:

$$X(\boldsymbol{F}_i, \boldsymbol{F}_j, 4) = -\frac{1}{24\pi}\int_S\int_S \boldsymbol{F}_i\cdot\boldsymbol{F}_j'|\boldsymbol{r}-\boldsymbol{r}'|^2 dS'dS \tag{51}$$

where $\boldsymbol{r}'$ is the position vector of the source point, and $\boldsymbol{F}_j'$ and dS' are with respect to $\boldsymbol{r}'$. From the chain rule and $\nabla\cdot\boldsymbol{F}_i = 0$, the following relation holds:

$$\nabla\cdot(\xi\boldsymbol{F}_i) = \hat{\xi}\cdot\boldsymbol{F}_i \tag{52}$$

where $\xi = x, y, z$, and $\hat{\xi}$ is the unit vector along the ξ-axis. Surface-integrating the both sides of (52) over S with respect to $\boldsymbol{r}$ and using the surface divergence theorem yields

$$\int_S \hat{\xi}\cdot\boldsymbol{F}_i dS = 0. \tag{53}$$

Therefore, the following relation holds:

$$\int_S \boldsymbol{F}_i dS = 0. \tag{54}$$

Similarly, the following relation also holds:

$$\int_S \boldsymbol{F}_j' dS' = 0. \tag{55}$$

Using $|\boldsymbol{r}-\boldsymbol{r}'|^2 = |\boldsymbol{r}|^2 - 2\boldsymbol{r}\cdot\boldsymbol{r}' + |\boldsymbol{r}'|^2$, (54), and (55), then (51) can be rewritten as follows:

$$X(\boldsymbol{F}_i, \boldsymbol{F}_j, 4) = \frac{1}{12\pi}\int_S\int_S\left(\boldsymbol{F}_i\cdot\boldsymbol{F}_j'\right)(\boldsymbol{r}\cdot\boldsymbol{r}')dS'dS. \tag{56}$$

To further transform (56), some other relations will be derived hereafter. First, from the vector triple product, the following relation holds:

$$\boldsymbol{r}\times\left(\boldsymbol{r}'\times\boldsymbol{F}_j'\right) = (\boldsymbol{F}_j'\cdot\boldsymbol{r})\boldsymbol{r}' - \boldsymbol{F}_j'(\boldsymbol{r}\cdot\boldsymbol{r}'). \tag{57}$$

Integrating the both sides of (57) yields

$$\begin{aligned}\int_S \boldsymbol{r}\times\left(\boldsymbol{r}'\times\boldsymbol{F}_j'\right)dS' &= \int_S\left(\boldsymbol{F}_j'\cdot\boldsymbol{r}\right)\boldsymbol{r}'dS'\\ &\quad - \int_S \boldsymbol{F}_j'\left(\boldsymbol{r}\cdot\boldsymbol{r}'\right)dS'.\end{aligned} \tag{58}$$

Besides, from the chain rule and $\nabla'\cdot\boldsymbol{F}_j' = 0$, the following relation holds:

$$\nabla'\cdot\left[\boldsymbol{F}_j'\left(\boldsymbol{r}\cdot\boldsymbol{r}'\right)\xi'\right] = \left(\boldsymbol{F}_j'\cdot\boldsymbol{r}\right)\xi' + \left(\boldsymbol{F}_j'\cdot\hat{\xi}\right)\left(\boldsymbol{r}\cdot\boldsymbol{r}'\right) \tag{59}$$

where $\xi = x, y, z$, and ξ' and ∇' are with respect to $\boldsymbol{r}'$. Surface-integrating the both sides of (59) over S with respect to $\boldsymbol{r}'$ and using the surface divergence theorem yields

$$\int_S\left(\boldsymbol{F}_j'\cdot\boldsymbol{r}\right)\xi'dS' + \int_S\left(\boldsymbol{F}_j'\cdot\hat{\xi}\right)\left(\boldsymbol{r}\cdot\boldsymbol{r}'\right)dS' = 0. \tag{60}$$

Therefore, the following relation holds:

$$\int_S (\boldsymbol{F}'_j \cdot \boldsymbol{r})\boldsymbol{r}' dS' + \int_S \boldsymbol{F}'_j (\boldsymbol{r} \cdot \boldsymbol{r}') dS' = 0. \tag{61}$$

Eliminating the term containing $(\boldsymbol{F}'_j \cdot \boldsymbol{r})\boldsymbol{r}'$ from (58) and (61) yields

$$\int_S \boldsymbol{F}'_j (\boldsymbol{r} \cdot \boldsymbol{r}') dS' = -\frac{1}{2}\int_S \boldsymbol{r} \times (\boldsymbol{r}' \times \boldsymbol{F}'_j) dS'. \tag{62}$$

Taking the dot product of both sides of (62) with $\boldsymbol{F}_i$, using the scalar triple product, and surface-integrating both sides over S with respect to $\boldsymbol{r}$ yields

$$\int_S \int_S (\boldsymbol{F}_i \cdot \boldsymbol{F}'_j)(\boldsymbol{r} \cdot \boldsymbol{r}') dS' = \frac{1}{2}\left(\int_S \boldsymbol{r} \times \boldsymbol{F}_i dS\right) \cdot \left(\int_S \boldsymbol{r}' \times \boldsymbol{F}'_j dS'\right). \tag{63}$$

Substituting (63) into (56) and removing the primes, then (42) is finally obtained. ∎

Acknowledgment

This work was performed in the Cooperative Research Project of the Research Institute of Electrical Communication, Tohoku University.

References

[1] *IEEE Standard for Definitions of Terms for Antennas*, Standard IEEE Std 145-2013 (Revision of IEEE Std 145-1993), Mar. 2014, pp. 1–50, doi: 10.1109/IEEESTD.2014.6758443.

[2] J. Lee and S. Nam, "Fundamental aspects of near-field coupling small antennas for wireless power transfer," *IEEE Trans. Antennas Propag.*, vol. 58, no. 11, pp. 3442–3449, Nov. 2010, doi: 10.1109/TAP.2010.2071330.

[3] Q. Chen, K. Ozawa, Q. Yuan, and K. Sawaya, "Antenna characterization for wireless power-transmission system using near-field coupling," *IEEE Antennas Propag. Mag.*, vol. 54, no. 4, pp. 108–116, Aug. 2012, doi: 10.1109/MAP.2012.6309161.

[4] A. Sharma, G. Singh, D. Bhatnagar, I. J. G. Zuazola, and A. Perallos, "Magnetic field forming using planar multicoil antenna to generate orthogonal H-field components," *IEEE Trans. Antennas Propag.*, vol. 65, no. 6, pp. 2906–2915, Jun. 2017, doi: 10.1109/TAP.2017.2695009.

[5] D. Vital and S. Bhardwaj, "Misalignment resilient anchor-shaped antennas in near-field wireless power transfer using electric and magnetic coupling modes," *IEEE Trans. Antennas Propag.*, vol. 69, no. 5, pp. 2513–2521, May 2021, doi: 10.1109/TAP.2020.3030976.

[6] R. W. P. King, C. W. Harrison, and D. H. Denton, "The electrically short antenna as a probe for measuring free electron densities and collision frequencies in an ionized region," *J. Res. Natl. Bur. Standards D. Radio Propag.*, vol. 65, no. 4, pp. 371–384, Jul. 1961.

[7] M. B. Kraichman, "Impedance of a circular loop in an infinite lossy dielectric," *J. Res. Natl. Bur. Standards D. Radio Propag.*, vol. 66D, no. 4, pp. 499–503, Jul. 1962.

[8] C. Yip, A. Goudevenos, and J. Lucas, "Antenna design for the propagation of EM waves in seawater," *Underwater Technol.*, vol. 28, no. 1, pp. 11–20, Nov. 2008, doi: 10.3723/ut.28.011.

[9] R. King, "Theory of the terminated insulated antenna in a conducting medium," *IEEE Trans. Antennas Propag.*, vol. AP-12, no. 3, pp. 305–318, May 1964, doi: 10.1109/TAP.1964.1138215.

[10] J. R. Wait, "Insulated loop antenna immersed in a lossy dielectric," *J. Res. Natl. Bur. Standards*, vol. 59, no. 2, pp. 133–137, Aug. 1957.

[11] T. Kawamura et al., "Formulae for the impedance and transmission factor of an electrically small half-sheath dipole antenna immersed in seawater," *IEEE Antennas Wireless Propag. Lett.*, vol. 21, pp. 640–644, 2022, doi: 10.1109/LAWP.2022.3141048.

[12] L. Yang, M. Ju, and B. Zhang, "Bidirectional undersea capacitive wireless power transfer system," *IEEE Access*, vol. 7, pp. 121046–121054, 2019, doi: 10.1109/ACCESS.2019.2937888.

[13] M. Tamura, K. Murai, and H. Matsukami, "Feasibility of electric double-layer coupler for wireless power transfer under seawater," *IEICE Trans. Electron.*, vol. E103.C, no. 6, pp. 308–316, Jun. 2020, doi: 10.1587/transele.2019ecp5033.

[14] T. Orekan, P. Zhang, and C. Shih, "Analysis, design, and maximum power-efficiency tracking for undersea wireless power transfer," *IEEE J. Emerg. Sel. Topics Power Electron.*, vol. 6, no. 2, pp. 843–854, Jun. 2018, doi: 10.1109/JESTPE.2017.2735964.

[15] R. Hasaba, K. Okamoto, S. Kawata, K. Eguchi, and Y. Koyanagi, "Magnetic resonance wireless power transfer over 10 m with multiple coils immersed in seawater," *IEEE Trans. Microw. Theory Techn.*, vol. 67, no. 11, pp. 4505–4513, Nov. 2019, doi: 10.1109/TMTT.2019.2928291.

[16] Y. Miyakozawa, T. Imura, and Y. Hori, "Frequency characteristics of wireless power transfer in seawater via magnetic resonant coupling," in *Proc. Asian Wireless Power Transf. Workshop*, Dec. 2022, pp. 115–118.

[17] N. Haga and M. Takahashi, "Circuit modeling technique for electrically-very-small devices based on laurent series expansion of self-/mutual impedances," *IEICE Trans. Commun.*, vol. E101, no. 2, pp. 555–563, Feb. 2018, doi: 10.1587/transcom.2017ebp3196.

[18] R. F. Harrington, *Field Computation by Moment Methods*. New York, NY, USA: Macmillan, 1965.

[19] N. Haga and M. Takahashi, "Circuit modeling of a wireless power transfer system by eigenmode analysis based on the impedance expansion method," *IEEE Trans. Antennas Propag.*, vol. 67, no. 2, pp. 1233–1245, Feb. 2019, doi: 10.1109/TAP.2018.2883632.

[20] N. Haga, J. Chakarothai, and K. Konno, "Circuit modeling of wireless power transfer system in the vicinity of perfectly conducting scatterer," *IEICE Trans. Commun.*, vol. E103.B, no. 12, pp. 1411–1420, Dec. 2020, doi: 10.1587/transcom.2019ebp3211.

[21] N. Haga, J. Chakarothai, and K. Konno, "Circuit modeling of a wireless power transfer system containing ferrite shields using an extended impedance expansion method," *IEEE Trans. Microw. Theory Techn.*, vol. 70, no. 5, pp. 2872–2881, May 2022, doi: 10.1109/TMTT.2022.3149830.

[22] A. E. Ruehli and H. Heeb, "Circuit models for three-dimensional geometries including dielectrics," *IEEE Trans. Microw. Theory Techn.*, vol. 40, no. 7, pp. 1507–1516, Jul. 1992, doi: 10.1109/22.146332.

[23] D. Gope, A. E. Ruehli, C. Yang, and V. Jandhyala, "(S)PEEC: Time- and frequency-domain surface formulation for modeling conductors and dielectrics in combined circuit electromagnetic simulations," *IEEE Trans. Microw. Theory Techn.*, vol. 54, no. 6, pp. 2453–2464, Jun. 2006, doi: 10.1109/TMTT.2006.875796.

[24] T. Campi, S. Cruciani, F. Palandrani, V. De Santis, A. Hirata, and M. Feliziani, "Wireless power transfer charging system for AIMDs and pacemakers," *IEEE Trans. Microw. Theory Techn.*, vol. 64, no. 2, pp. 633–642, Feb. 2016, doi: 10.1109/TMTT.2015.2511011.

[25] C. Xiao, K. Wei, D. Cheng, and Y. Liu, "Wireless charging system considering eddy current in cardiac pacemaker shell: Theoretical modeling, experiments, and safety simulations," *IEEE Trans. Ind. Electron.*, vol. 64, no. 5, pp. 3978–3988, May 2017, doi: 10.1109/TIE.2016.2645142.

[26] M. A. Callejon, D. Naranjo-Hernandez, J. Reina-Tosina, and L. M. Roa, "Distributed circuit modeling of galvanic and capacitive coupling for intrabody communication," *IEEE Trans. Biomed. Eng.*, vol. 59, no. 11, pp. 3263–3269, Nov. 2012, doi: 10.1109/TBME.2012.2205382.

[27] N. Haga, K. Saito, M. Takahashi, and K. Ito, "Equivalent circuit of intrabody communication channels inducing conduction currents inside the human body," *IEEE Trans. Antennas Propag.*, vol. 61, no. 5, pp. 2807–2816, May 2013, doi: 10.1109/TAP.2013.2246534.

[28] Y. Nishida, K. Sasaki, K. Yamamoto, D. Muramatsu, and F. Koshiji, "Equivalent circuit model viewed from receiver side in human body communication," *IEEE Trans. Biomed. Circuits Syst.*, vol. 13, no. 4, pp. 746–755, Aug. 2019, doi: 10.1109/TBCAS.2019.2918323.

[29] I. I. Smolyaninov, Q. Balzano, C. C. Davis, and D. Young, "Surface wave based underwater radio communication," *IEEE Antennas Wireless Propag. Lett.*, vol. 17, no. 12, pp. 2503–2507, Dec. 2018, doi: 10.1109/LAWP.2018.2880008.

[30] R. Kato, M. Takahashi, N. Ishii, Q. Chen, and H. Yoshida, "Investigation of a 3-D undersea positioning system using electromagnetic waves," *IEEE Trans. Antennas Propag.*, vol. 69, no. 8, pp. 4967–4974, Aug. 2021, doi: 10.1109/TAP.2020.3048584.

[31] K. Umashankar, A. Taflove, and S. Rao, "Electromagnetic scattering by arbitrary shaped three-dimensional homogeneous lossy dielectric objects," *IEEE Trans. Antennas Propag.*, vol. AP-34, no. 6, pp. 758–766, Jun. 1986, doi: 10.1109/TAP.1986.1143894.

[32] S. Y. Chen, W. Cho Chew, J. M. Song, and J.-S. Zhao, "Analysis of low frequency scattering from penetrable scatterers," *IEEE Trans. Geosci. Remote Sens.*, vol. 39, no. 4, pp. 726–735, Apr. 2001, doi: 10.1109/36.917883.

[33] S. Chen, J.-S. Zhao, and W. C. Chew, "Analyzing low-frequency electromagnetic scattering from a composite object," *IEEE Trans. Geosci. Remote Sens.*, vol. 40, no. 2, pp. 426–433, Feb. 2002, doi: 10.1109/36.992806.

[34] N. Ishii, Y. Shimizu, J. Chakarothai, K. Wake, and S. Watanabe, "An extension of probe calibration method for SAR measurement to the kHz band," in *Proc. Int. Symp. Antennas Propag. (ISAP)*, Oct. 2019, pp. 1–3.

[35] K. Yee, "Numerical solution of initial boundary value problems involving Maxwell's equations in isotropic media," *IEEE Trans. Antennas Propag.*, vol. AP-14, no. 3, pp. 302–307, May 1966, doi: 10.1109/TAP.1966.1138693.

[36] J. Van Bladel, "Stevenson's method applied to good conductors," in *Electromagnetic Fields*, 2nd ed., Hoboken, NJ, USA: Wiley, 2007, ch. 13, sec. 10, pp. 711–715.

[37] A. Karlsson, "Physical limitations of antennas in a lossy medium," *IEEE Trans. Antennas Propag.*, vol. 52, no. 8, pp. 2027–2033, Aug. 2004, doi: 10.1109/TAP.2004.832335.

Nozomi Haga (Member, IEEE) was born in Yamagata, Japan, in January 1985. He received the B.E., M.E., and D.E. degrees from Chiba University, Chiba, Japan, in 2007, 2009, and 2012, respectively.

From 2012 to 2023, he was an Assistant Professor at the Graduate School of Science and Technology, Gunma University, Gunma, Japan. Since 2023, he has been an Associate Professor at the Department of Electrical and Electronic Information Engineering, Toyohashi University of Technology, Toyohashi, Japan. His main interests include electrically small antennas, body-centric wireless communication channels, and wireless power transfer systems.

Dr. Haga received the IEICE Technical Committee on Antennas and Propagation: Young Researcher Award in 2012, the IEICE Technical Committee on Wireless Power Transfer: Young Researcher Award in 2018, and the IEEE Antennas and Propagation Society Japan Young Engineer Award in 2018.

Jerdvisanop Chakarothai (Senior Member, IEEE) received the B.E. degree in electrical and electronic engineering from Akita University, Akita, Japan, in 2003, and the M.E. and D.E. degrees in electrical and communications engineering from Tohoku University, Sendai, Japan, in 2005 and 2010, respectively.

He was a Research Associate at Tohoku University in 2010, before joining the Nagoya Institute of Technology, Nagoya, Japan, and Tokyo Metropolitan University, Tokyo, Japan, in 2011 and 2013, respectively. He is currently with the National Institute of Information and Communications Technology, Tokyo, Japan. His research interests include computational electromagnetics (CEM) for biomedical communications and electromagnetic compatibility, measurement, and calibration methods for electromagnetic interference.

Dr. Chakarothai is a member of the Institute of Electronics, Information and Communication Engineers (IEICE) and the Institute of Electrical Engineers (IEE), Japan. He is also a member of the Bioelectromagnetic Society and the Applied Computational Electromagnetic Society. He received the 2014 Young Scientist Award from the International Scientific Radio Union and the 2018 Ulrich L. Rohde Innovative Conference Paper Award on Antenna Measurements and Applications.

Keisuke Konno (Member, IEEE) received the B.E., M.E., and D.E. degrees from Tohoku University, Sendai, Japan, in 2007, 2009, and 2012, respectively.

Since 2012, he has been with the Department of Communications Engineering, Graduate School of Engineering, Tohoku University, where he is an Associate Professor. He received a JSPS Postdoctoral Fellowship for Research Abroad and he was staying with the ElectroScience Laboratory, The Ohio State University, Columbus, OH, USA, as a Visiting Scholar from 2015 to 2017. His research interests include computational electromagnetics, array antennas, reflectarrays, and source reconstruction.

Dr. Konno is a member of IEICE. He received the Encouragement Award for Young Researcher and Most Frequent Presentations Award in 2010 from the Technical Committee on Antennas and Propagation of Japan, Young Researchers Award in 2011 from the Institute of Electronics, Information and Communication Engineers (IEICE) of Japan, IEEE EMC Society Sendai Chapter Student Brush-up Session and EMC Sendai Seminar Student Best Presentation Award in 2011, JSPS Washington Director Award in 2016, MHz Rectenna Award in 2017, Young Researchers Award for ECEI of Tohoku University in 2018, Minoru Ishida Award in 2018, IEEE AP-S Japan Young Engineer Award in 2018, and TOKIN Foundation Research Encouragement Award in 2019.